Published in final edited form as:
Nat Genet. 2022 August 01; 54(8): 1214–1226. doi:10.1038/s41588-022-01120-0.

Loss of FOCAD, operating via the SKI messenger RNA surveillance pathway, causes a pediatric syndrome with liver cirrhosis

Ricardo Moreno Traspas[1,2,✉], **Tze Shin Teoh**[1,2], **Pui-Mun Wong**[1], **Michael Maier**[1], **Crystal Y. Chia**[1], **Kenneth Lay**[1], **Nur Ain Ali**[1], **Austin Larson**[3], **Fuad Al Mutairi**[4,5], **Nouriya Abbas Al-Sannaa**[6], **Eissa Ali Faqeih**[7], **Majid Alfadhel**[4,8], **Huma Arshad Cheema**[9], **Juliette Dupont**[10], **Stéphane Bézieau**[11], **Bertrand Isidor**[11], **Dorrain Yanwen Low**[12], **Yulan Wang**[12], **Grace Tan**[2], **Poh San Lai**[2], **Hugues Piloquet**[13], **Madeleine Joubert**[14], **Hulya Kayserili**[15], **Kimberly A. Kripps**[16], **Shareef A. Nahas**[17], **Eric P. Wartchow**[18], **Mikako Warren**[19], **Gandham SriLakshmi Bhavani**[20], **Majed Dasouki**[21], **Renata Sandoval**[22], **Elisa Carvalho**[23], **Luiza Ramos**[24], **Gilda Porta**[25], **Bin Wu**[26,27], **Harsha Prasada Lashkari**[28,29], **Badr AlSaleem**[30], **Raeda M. BaAbbad**[30], **Anabela Natália Abreu Ferrão**[31], **Vasiliki Karageorgou**[32], **Natalia Ordonez-Herrera**[32], **Suliman Khan**[32], **Peter Bauer**[32], **Benjamin Cogne**[11], **Aida M. Bertoli-Avella**[32], **Marie Vincent**[11], **Katta Mohan Girisha**[20], **Bruno Reversade**[1,2,15,33,34,✉]

[1]Laboratory of Human Genetics and Therapeutics, Genome Institute of Singapore, A*STAR, Singapore, Singapore

[2]Department of Pediatrics, Yong Loo Lin School of Medicine, National University of Singapore, Singapore, Singapore

[3]Section of Pediatrics-Clinical Genetics and Metabolism, Children's Hospital Colorado, Aurora, CO, USA

[4]Department of Genetics and Precision Medicine, King Abdullah Specialized Children Hospital, King Abdulaziz Medical City, Ministry of National Guard Health Affairs, Riyadh, Saudi Arabia

✉**Correspondence and requests for materials** should be addressed to Ricardo Moreno Traspas or Bruno Reversade. ricardo.traspas@reversade.com; bruno@reversade.com.

Author contributions

B.R., K.M.G., M.V. and B.C. initiated the study. B.R. and R.M.T. designed the study. B.R. and P.-M.W. supervised the study. B.R., P.B., A.M.B.-A., V.K., N.O.-H., S.K., M.A. and H.K. coordinated the clinical part of the study. K.M.G., M.V., B.C., A.L., F.A.M., N.A.A.-S., E.A.F., H.A.C., J.D., S.B., B.I., H.P., M.J., K.A.K., S.A.N., E.P.W., M.W., G.S.B., M.D., R.S., E.C., L.R., G.P., H.P.L., B.A., R.M.B. and A.N.A.F. conducted the clinical and genetic evaluation of the patients, the collection of human biological samples and the trio whole genome/exome sequencing for the corresponding affected family. R.M.T. designed and performed all the biochemical, cell culture and in vivo experiments, with help from B.R., T.S.T., P.-M.W., M.M., K.L., N.A.A. and C.Y.C. D.Y.L. and Y.W. conducted the lipidomics analysis on zebrafish livers. G.T. and P.S.L. conducted the clinical curation of the *FOCAD* variants. B.W. performed the structural analysis of the missense *FOCAD* variants. R.M.T. conducted all the rest of the data processing and analysis. B.R. and R.M.T. wrote the manuscript with input from all co-authors and performed all revisions.

Competing interests

P.B., A.M.B.-A., V.K., N.O.-H. and S.K. are employed by and receive a salary from Centogene AG (exome sequencing is among the commercially available tests). K.M.G. is founder and director of Suma Genomics (exome sequencing is among the commercially available tests). The remaining authors declare no competing interests.

Peer review information *Nature Genetics* thanks Alexandre Fabre and Paul Gissen for their contribution to the peer review of this work. Peer reviewer reports are available.

Europe PMC Funders Author Manuscripts

[5]College of Medicine, King Saud bin Abdulaziz University for Health Sciences, King Abdulaziz Medical City, Ministry of National Guard Health Affairs, Riyadh, Saudi Arabia

[6]Pediatric Services, John Hopkins Aramco Healthcare, Dhahran, Saudi Arabia

[7]Section of Medical Genetics, Children's Specialist Hospital, King Fahad Medical City, Riyadh, Saudi Arabia

[8]Department of Medical Genomic Research, King Abdullah International Medical Research Centre, King Saud bin Abdulaziz University for Health Sciences, King Abdulaziz Medical City, Ministry of National Guard Health Affairs, Riyadh, Saudi Arabia

[9]Division of Pediatric Gastroenterology-Hepatology and Nutrition, The Children's Hospital and The Institute of Child Health, Lahore, Pakistan

[10]Department of Pediatrics, Genetic Services, Lisbon North University Hospital Center, Lisbon, Portugal

[11]Medical Genetics Service, Nantes University Hospital Center, Nantes, France

[12]Singapore Phenome Center, Lee Kong Chian School of Medicine, Nanyang Technological University, Singapore, Singapore

[13]Gastropediatrics Department, Nantes University Hospital Center, Nantes, France

[14]Anatomopathology Department, Nantes University Hospital Center, Nantes, France

[15]Medical Genetics Department, School of Medicine, Koç University, Istanbul, Turkey

[16]Department of Molecular and Medical Genetics, Oregon Health and Science University, Portland, OR, USA

[17]Rady Children's Institute for Genomic Medicine, San Diego, CA, USA

[18]Department of Pathology and Laboratory Medicine, Children's Hospital Colorado, Aurora, CO, USA

[19]Department of Pathology and Laboratory Medicine, Children's Hospital Los Angeles, University of Southern California Keck School of Medicine, Los Angeles, CA, USA

[20]Department of Medical Genetics, Kasturba Medical College, Manipal Academy of Higher Education, Manipal, India

[21]Department of Pediatric Genetics, AdventHealth Medical Group, Orlando, FL, USA

[22]Department of Oncogenetics, Hospital Sírio-Libanês, Brasília, Brazil

[23]Department of Pediatric Gastroenterology and Hepatology, Hospital da Criança de Brasília José Alencar, UniCEUB, Brasília, Brazil

[24]Mendelics Genomic Analysis, São Paulo, Brazil

[25]Department of Pediatric Hepatology, Transplant Unit, Hospital Sírio-Libanês, São Paulo, Brazil

[26]School of Biological Sciences, Nanyang Technological University, Singapore, Singapore

[27]Institute of Structural Biology, Nanyang Technological University, Singapore, Singapore

[28]Department of Pediatrics, Kasturba Medical College, Mangalore, India

[29]Manipal Academy of Higher Education, Manipal, India

[30]Section of Pediatric Gastroenterology-Hepatology, Children's Specialist Hospital, King Fahad Medical City, Riyadh, Saudi Arabia

[31]Department of Pediatrics, Hematology Unit, Lisbon North University Hospital Center, Lisbon, Portugal

[32]Centogene AG, Rostock, Germany

[33]Institute of Molecular and Cell Biology, A*STAR, Singapore, Singapore

[34]Smart-Health Initiative, Biological and Environmental Sciences and Engineering Division, King Abdullah University of Science and Technology (KAUST), Thuwal, Saudi Arabia

Europe PMC Funders Author Manuscripts

Abstract

Cirrhosis is usually a late-onset and life-threatening disease characterized by fibrotic scarring and inflammation that disrupts liver architecture and function. While it is typically the result of alcoholism or hepatitis viral infection in adults, its etiology in infants is much less understood. In this study, we report 14 children from ten unrelated families presenting with a syndromic form of pediatric liver cirrhosis. By genome/exome sequencing, we found recessive variants in *FOCAD* segregating with the disease. Zebrafish lacking *focad* phenocopied the human disease, revealing a signature of altered messenger RNA (mRNA) degradation processes in the liver. Using patient's primary cells and CRISPR-Cas9-mediated inactivation in human hepatic cell lines, we found that FOCAD deficiency compromises the SKI mRNA surveillance pathway by reducing the levels of the RNA helicase SKIC2 and its cofactor SKIC3. FOCAD knockout hepatocytes exhibited lowered albumin expression and signs of persistent injury accompanied by CCL2 overproduction. Our results reveal the importance of FOCAD in maintaining liver homeostasis and disclose a possible therapeutic intervention point via inhibition of the CCL2/CCR2 signaling axis.

The human liver is endowed with intrinsic capability to regenerate upon injury. However, when damage and inflammation persist, the organ may lose its regenerative potential, leading to irreversible cirrhosis[1–3]. Injured hepatocytes release reactive oxygen species, inflammatory signals and profibrotic mediators that promote the recruitment of leukocytes, the capillarization of sinusoids and the activation of quiescent hepatic stellate cells (HSCs). Activated HSCs differentiate into myofibroblasts that synthesize extracellular matrix (ECM) as part of a fibrogenic response[1–6]. Fibrosis, which is a reversible process, may evolve to hepatic cirrhosis if unresolved. Cirrhotic livers are characterized by the disruption of the tissue architecture due to the formation of regenerative nodules of hepatocytes surrounded by large fibrous scars, which compromise the homeostasis and normal function of the organ[7]. Cirrhosis remains chronic for the rest of the patient's life and may lead to portal hypertension, hepatic encephalopathy and the development of hepatocellular carcinoma (HCC). End-stage liver cirrhosis is increasingly becoming a main health and economic burden to society, causing more than 1 million deaths globally each year[8,9]. Despite extensive research, there are still no effective drugs or therapies to combat the disease.

To this day, liver transplant remains the gold standard treatment for decompensated liver cirrhosis[10].

The etiology of liver cirrhosis originates mainly from environmental insults, but little has been done to identify the genetic underpinnings on which these environmental cues operate. To address this problem, we used the power of Mendelian genetics as a means to identify single-gene defects responsible for liver diseases in humans. Through an extensive network of clinicians and scientists, we identified a total of 14 children from seven countries presenting with a multisystemic syndrome characterized by severe neonatal liver cirrhosis. All cases were found to segregate germline recessive mutations in *FOCAD* (MIM614606)—a gene with no previously reported links to liver biology. Using CRISPR-Cas9 technology, we generated in vitro and in vivo *FOCAD*-knockout biological platforms that helped to delineate the cellular and molecular basis of this neonatal liver disease.

The nascent literature on FOCAD's biological function is scarce and fraught with contradictions, having been implicated in focal adhesions, microtubule dynamics, cell cycle control and cancer predisposition[11–14]. Our unbiased transcriptomic analysis of livers from *focad-knockout* zebrafish pointed instead towards a defective SKI mRNA surveillance pathway. The SKI multiprotein complex was initially discovered in yeast as a host-directed antiviral mechanism that targets double-stranded viral RNA for degradation[15–17]. In a manner similar to the role of the proteasome in protein degradation, the SKI complex, consisting of helicase SKIC2 (previously known as SKIV2L) and its cofactors SKIC3 (previously known as TTC37) and SKIC8 (previously known as WDR61), forms a macromolecular assembly that associates with the cytoplasmic exosome to degrade RNA molecules[18–20]. Tuck et al.21 reported that SKIC2 possesses two additional cofactors: FOCAD and AVEN. Whereas they proposed that AVEN acts cooperatively with the SKI complex in translation surveillance by preventing ribosome stalling, the exact role of FOCAD is not understood[21]. Here we show that FOCAD is essential for maintaining the proteostatic levels of SKIC2 and SKIC3 in various human cell lines and in an animal model of the disease. The notable clinical overlap between *FOCAD* deficiency and tricho-hepato-enteric syndromes (THES) caused by mutations in *SKIC2* or *SKIC3* lends credence to the notion that FOCAD is directly involved in the SKI mRNA surveillance pathway.

Results

Identification of 14 patients with biallelic *FOCAD* mutations

Liver cirrhosis is generally regarded as a late-onset disease that manifests in adults following environmental insults such as viral infection, a high-fat diet or chronic alcohol abuse[1–3,7]. Rarely have there been reports of early-onset forms of the disease. When diagnosed in children, it is usually caused by mitochondrial hepatopathies[22], hereditary cholangiopathies[23] or glycogen storage diseases[24]. In a collaborative effort involving clinicians and scientists from different continents, we identified 14 affected children presenting with a common core phenotype consisting of severe congenital liver disease (Fig. 1a, Supplementary Table 1 and Supplementary Note). All the patients were below 15 years of age and belonged to ten unrelated families from different geographical regions. The liver phenotype was marked by cirrhosis (71.4%) with multinodularity (57.1%), as confirmed by

ultrasonography, magnetic resonance imaging and liver needle biopsies (Fig. 1b–e, Extended Data Fig. 1b, Supplementary Table 1 and Supplementary Note). Intrahepatic cholestasis was diagnosed in 35.7% of the patients, with associated jaundice (35.7%) and biliary hyperplasia (28.6%) (Supplementary Table 1 and Supplementary Note). Portal hypertension complications were also observed, including splenomegaly (71.4%) and ascites (28.6%) (Supplementary Table 1 and Supplementary Note). The presence of hepatomegaly (71.4%), hypoalbuminemia (71.4%), elevated circulating hepatic enzymes (71.4%) and elevated circulating alpha-fetoprotein (42.9%) in most patients evinced liver dysfunction, injury and inflammation (Supplementary Table 1 and Supplementary Note). In some subjects, hepatic metabolic alterations, such as steatosis (21.4%) (Fig. 1d and Extended Data Fig. 1b), increased glycogen content (14.3%) (Fig. 1e and Extended Data Fig. 1b) and iron overload (21.4%), were also recorded (Supplementary Table 1 and Supplementary Note). Patient F3-II:1 underwent liver transplantation at 6 months of age (Fig. 1b), succumbing to multiorgan failure 2 weeks thereafter (Fig. 1a, Supplementary Table 1 and Supplementary Note).

Although the liver was the organ affected most severely in all the patients, additional clinical manifestations with medium-to-low penetrance were also documented. All the patients presented with gastrointestinal alterations, including abdominal distension (78.6%), diarrhea (57.1%, nutritional support was required in only one of the patients), feeding difficulties (42.9%), inguinal hernia (42.9%) and umbilical hernia (35.7%) (Supplementary Table 1 and Supplementary Note). Other clinical findings detected in more than half of the subjects were metabolic anomalies (85.7%), intrauterine growth restriction (IUGR) (64.3%) and blood disorders (64.3%) (Supplementary Table 1 and Supplementary Note). The respiratory system was found compromised in 50% of the affected children, while congenital cardiac defects and genitourinary abnormalities were reported with a prevalence of 42.9% (Supplementary Table 1 and Supplementary Note). Most of the children (71.4%) showed slow physical growth and difficulties gaining weight, especially in the first 2 years of life (Supplementary Table 1 and Supplementary Note). Although the overall physical appearance of most of the patients was normal, mild facial abnormalities were present in 5 probands from F2, F5, F9 and F10 (Extended Data Fig. 1a, Supplementary Table 1 and Supplementary Note). Neurological abnormalities were rare and nonspecific (Supplementary Table 1 and Supplementary Note). Of the 14 affected children, 6 passed away (F3-II:1, F4-II:1, F6-II:3, F6-II:6, F7-II:3, F8-II:3) due to hepatic or multiorgan failure (Fig. 1a, Supplementary Table 1 and Supplementary Note), 5 of them before the age of 1 year.

To identify the underlying genetic cause of this pediatric liver syndrome, we performed trio genome or exome sequencing in parents and affected individuals from all ten families. Mendelian recessive inheritance was favored by the consanguineous backgrounds of six of the families, allowing us to focus on homozygous or compound heterozygous variants present in the affected children. Distinct germline recessive mutations in *FOCAD* (MIM614606) were found in all families and fully segregated with the disease (Figs. 1a and 2a and Supplementary Table 1). Patients from families F1, F2 and F3 carried compound heterozygous *FOCAD* variants, whereas patients from families F4, F5, F6, F7, F8, F9 and F10 were homozygotes (Figs. 1a and 2a and Supplementary Table 1). Germline monoallelic

and somatic *FOCAD* mutations have been previously associated with the development of glioma and other cancers[11,13], but no links to liver diseases have been documented.

FOCAD variants are loss-of-function alleles

FOCAD codes for FOCADHESIN (Q5VW36), a poorly characterized protein whose exact function and structure remain unknown. UniProt and SWISS-MODEL predict the presence of three possible transmembrane domains between amino acids 404–424, 441–461 and 1036–1056, while two domains of unknown function DUF3037 and DUF3028 can be delineated (Fig. 2a). DUF3037 is highly conserved across all metazoa and in ancient amoebozoa[25]. We identified a total of 14 germline mutations in the ten recruited families, which spanned the entire protein and included three stop-gain variants (*m1*: c.2587 C > T, p.Arg863*; *m8*: c.583 C > T, p.Arg195*; *m11*: c.460 C > T, p.Gln154*), two frameshift alleles resulting in early stop codons (*m4*: c.2675dupC, p.Trp893Leufs*32; *m9*: c.4343delT, p.Leu1448Cysfs*3), one large deletion of 164.8 kb encompassing exons 14–37 (*m6*: c.1820-24876_4496 + 6663del), five mutations affecting splicing as predicted by the Human Splicing Finder software[26] (*m3*: c.5004 G >C (disrupted donor site); *m5*: c.58-1 G > C (disrupted acceptor site); *m10*: c.3529 G > A (activation of a cryptic acceptor site); *m12*: c.2107-1 G > A (disrupted acceptor site); *m13*: c.1662 + 1 G > A (disrupted donor site)) and three missense variants in highly conserved residues (*m2*(*a*): c.1687C > T, p.Arg563Cys; *m2*(*b*): c.3694 G > C, p.Ala1232Pro; *m7*: c.5339 T > C, p.Leu1780Pro) (Figs. 1a and 2a,b and Supplementary Table 2). Four of these variants (*m2*(*a*), *m8*, *m10*, *m11*) are annotated in public databases (ExAC, gnomAD, BRAVO/TOPmed) with very low frequencies (minor allele frequency $\leq 10^{-4}$) at the homozygous state, suggesting that undiagnosed cases exist in these patient cohorts (Fig. 1f and Supplementary Table 2). The remaining genetic alterations reported in this study (*m1*, *m2*(*b*), *m3*, *m4*, *m5*, *m6*, *m7*, *m9*, *m12*, *m13*) are private mutations (Fig. 1f and Supplementary Table 2). All FOCAD variants showed high combined annotation-dependent depletion (CADD) scores above 19 (Fig. 1f and Supplementary Table 2) and DANN scores above 0.96 (Supplementary Table 2), indicating that they are predicted to be highly damaging. The MutationTaster software predicted all mutations to be disease-causing (Supplementary Table 2). The three missense variants were also tested using the SIFT and Polyphen2 prediction software, yielding similar results (Supplementary Table 2). According to AlphaFold2 (ref. [27]), mutated residues at positions p.Arg563, p.Ala1232 and p.Leu1780 are predicted with high confidence to be part of α-helical regions (Fig. 2c). In particular, p.Ala1232Pro (*m2*(*b*)) and p.Leu1780Pro (*m7*) mutations are expected to seriously disrupt α-helices and, consequently, destabilize their stacking within the FOCAD protein. While the missense p.Arg563Cys (*m2*(*a*)) mutant is not obviously disrupting the tertiary structure of FOCAD, it is located at a peripheral surface that might be responsible for interacting with other potential binding partners.

FOCAD has a residual variation intolerance score (RVIS) of −0.19 (placing it in the top 39% of human genes most intolerant to genetic variation) and a predicted loss-of-function (pLOF) observed/expected score of 0.72 (gnomAD), suggesting that *FOCAD* loss-of-function is under negative selection. Overall, our in silico analysis data and the recessive mode of inheritance of the disease argue that the identified *FOCAD* variants are most likely loss-of-function alleles.

focad knockout in zebrafish phenocopies the human liver disorder

To investigate the contribution of FOCAD to liver biology, we sought to develop a knockout animal model using CRISPR-Cas9 engineering. FOCAD presents a highly conserved amino acid sequence in all vertebrate species, and the zebrafish genome contains a single *focad* homolog situated on chromosome 7. Guide RNAs against exon 4 were designed and microinjected together with Cas9 mRNA into zebrafish zygotes (Extended Data Fig. 2a). We identified, selected and outcrossed two mutant lines transmitting out-of-frame *focad* deletions of 7 base pairs (bp) (*focad*$^{\Delta 7}$) and 8 bp (*focad*$^{\Delta 8}$) (Extended Data Fig. 2a). Homozygous *focad-null* fish embryos developed into phenotypically normal and fertile adults that could be inbred to generate complete maternal zygotic (*MZ*) null fish. As *focad* mRNA is maternally contributed (Extended Data Fig. 2b), *MZ* null adult animals were used for our phenotypic characterization studies. Quantitative PCR with reverse transcription (RT-qPCR) performed on livers from *MZ focad*$^{\Delta 7/\Delta 7}$ fish showed a statistically significant 75% reduction in endogenous *focad* mRNA levels (Fig. 3e), suggesting that the mutant transcript undergoes nonsense-mediated decay (NMD). Absence of endogenous Focad protein in the knockout animals was confirmed by western blotting on brain extracts (Fig. 3f). At 70 days postfertilization, the survival rate of *MZ focad*$^{\Delta 7/\Delta 7}$ fish (49%) was significantly lower compared with *focad*$^{+/\Delta 7}$ siblings (76%), indicating that the complete loss of *focad* compromises organismal survival (Fig. 3d). Growth retardation was also documented, which phenocopies the failure to thrive observed in most *FOCAD*-deficient patients. *MZ focad*$^{\Delta 7/\Delta 7}$ fish were significantly smaller both in terms of weight and length compared with heterozygous fish at 3 months of age (Fig. 3a,b). With a constant body mass index (BMI), Focad-null fish were proportionally smaller (Fig. 3b) and showed signs of subfertility (Fig. 3c). Histological assessment of liver sections from adult *MZ focad*$^{\Delta 7/\Delta 7}$ fish by hematoxylin and eosin (H&E) staining revealed a pathological tissue architecture with swollen hepatocytes and signs of steatosis (Fig. 3g). Masson's trichrome staining showed a general increase in collagen, a hallmark of hepatic fibrosis (Fig. 3g), with significant hepatocyte apoptosis revealed by TUNEL staining (Fig. 3h). As metabolomic derangement is a distinctive feature of liver diseases[28,29], we performed a lipidomics analysis on livers from wild-type (*WT*) and *MZ focad*$^{\Delta 7/\Delta 7}$ fish at 3 months of age. The orthogonal projections to latent structures discriminant analysis (OPLS-DA) showed that the hepatic phospholipid profiles of each genotype were well separated (Fig. 4a). Our results unraveled the dysregulation of multiple lipid species with high correlation coefficients (≥0.5) in *focad*-null livers, suggestive of a hepatic steatosis phenotype (Fig. 4b). To obtain an unbiased picture of the transcriptome of hepatic tissues lacking Focad, we carried out mRNA-sequencing (RNA-seq) analyses on *WT* and *MZ focad*$^{\Delta 7/\Delta 7}$ adult livers (GEO accession: GSE168961). Cluster analysis of differentially expressed genes (DEGs) showed a clear separation between both genotypes (Fig. 4c), with a total of 68 significantly upregulated ($\log_2$(fold change) > 3, $-\log_{10}(P_{adj})$ > 2.5) and 100 significantly downregulated ($\log_2$(fold change) < –3, $-\log_{10}(P_{adj})$ > 2.5) DEGs (Fig. 4f). Among the top dysregulated hits, genes related to liver function (*urahb*, *cyp3c2*), fibrosis (*mfap4.12*, *lgals8b*, *coch*) and injury (*sh3bp5b*) were prominently featured (Fig. 4f and Supplementary Table 3). RT-qPCR was used for orthogonal validation of the RNA-seq data (Fig. 4g), which also revealed a tenfold upregulation of *serum amyloid A* (*saa*) expression (Fig. 4g), indicative of severe hepatic inflammation[30]. Gene ontology (GO) and Kyoto Encyclopedia of Genes and Genomes (KEGG) enrichment

analysis of the DEGs provided further evidence of an underlying acute immune response in *focad-null* livers (GO:0006955, GO:0002376, dre04620, dre04621, dre04060), as well as abnormalities in redox (GO:0055114, GO:0016705), iron physiology (GO:0006826, GO:0015093, GO:0015684, GO:0005381, GO:0020037, GO:0005506, GO:0046906) and liver metabolic processes (dre00120, dre00350, dre00330) (Fig. 4d,e and Supplementary Tables 4 and 5). These results provide a molecular insight into the liver phenotype of *focad*-deficient fish, which is characterized by oxidative stress, inflammation and iron metabolic alterations. Our in vivo disease modeling efforts demonstrate that the loss of *focad* is sufficient to induce hepatic injury in distantly related organisms, suggesting that FOCAD plays a pivotal role in maintaining liver homeostasis across vertebrate species.

Whereas most GO terms and KEGG pathways were related to common and well-known features of liver disease, transcripts linked to RNA biology such as RNA binding (GO:0003723), RNA helicase activity (GO:0003724), RNA degradation (dre03018) and the mRNA surveillance pathway (dre03015) were conspicuously altered in *focad*-deficient livers (Fig. 3d–g and Supplementary Tables 3–5). This seemed to be a distinctive feature of this syndrome, which connects aberrant RNA biological processes to liver function. In support of this link are the recent findings by Tuck et al.[21], who reported a direct binding of FOCAD to SKIC2, the RNA helicase of the SKI pathway. Although the exact role of FOCAD in this 3′ to 5′ mRNA decay pathway is unclear, our in vivo data points to a defective SKI-mediated mRNA degradation pathway as a potential molecular signature in *FOCAD*-deficient hepatic tissues.

FOCAD absence compromises SKIC2 and SKIC3 protein levels

To better delineate the cellular function of FOCAD, we pivoted to an in vitro system using patient-derived cells and human hepatic cell types. The nascent literature on FOCAD biology remains controversial. Despite being predicted (UniProt, SWISS-MODEL) to contain three transmembrane domains, there is no experimental evidence that FOCAD localizes in organelles with bilayered lipid membranes. Conflicting studies have reported detecting FOCAD in focal adhesions[11], centrosomes[12] and mitochondria (https://www.proteinatlas.org). To clarify this, we first analyzed FOCAD's cellular localization by immunofluorescence in a HEK293T overexpression system, using an N-terminally tagged MYC construct. We observed a homogenous cytosolic signal (Fig. 5a), which did not resemble focal adhesions or centrosomes. The staining was analogous to its SKI complex interactor SKIC2 (refs. [31–33]). Aiming to confirm these results with endogenous protein, we performed subcellular fractionation in human primary dermal fibroblasts. Western blot results showed FOCAD enrichment in the cytosolic extract, but not in the endoplasmic reticulum/Golgi apparatus/mitochondria (ER/Golgi/Mito) or nuclear fractions (Fig. 5b). These data indicated that FOCAD is predominantly cytosolic, which is in line with the localization of the SKI complex.

We next made use of primary dermal fibroblasts from patients F1-II:1 (*m1*, *m2*) and F2-II:2 (*m3*, *m4*) to examine the pathogenicity of the identified germline variants. RT-qPCR data revealed comparable endogenous *FOCAD* transcript levels in F1-II:1 and two unrelated WT individuals, but statistically significantly reduced levels in F2-II:2 (Fig. 5c). Protein

expression analysis by western blot revealed that endogenous FOCAD was nearly absent in the cellular extracts of both patients (Fig. 5d). These results indicate that the compound heterozygous *FOCAD* mutant variants in F1 and F2 behave as protein-null alleles, providing experimental evidence for our in silico predictions (Fig. 1f and Supplementary Table 2). Analysis of endogenous SKIC2 protein revealed drastically diminished levels in the cells of the patients, suggesting that FOCAD may contribute to the stability of this RNA helicase (Fig. 5d). To confirm this finding with disease-relevant cells, we employed CRISPR-Cas9 to specifically knockout *FOCAD* in human LX-2 HSCs[34] and Hc3716-hTERT hepatocytes[35], which represent the two main cell types found in the liver. Similar to our data in patient-derived primary dermal fibroblasts, *FOCAD*-deficient HSCs and hepatocytes led to a marked reduction of endogenous SKIC2 protein levels that paralleled the loss of FOCAD (Fig. 6a,d). SKIC3 and SKIC8, the two additional components of the SKI complex, also seemed to respond to the loss of FOCAD, with endogenous SKIC3 levels being nearly halved (Fig. 6a,d). These results indicated that FOCAD is essential to maintain the proteostatic levels of SKIC2 and SKIC3 in all three human cell types tested.

Loss of FOCAD disrupts hepatocyte homeostasis

In the context of hepatocyte damage, quiescent HSCs become activated and transdifferentiate into myofibroblasts that express *ACTA2* and *CTGF*, as well as ECM components such as *COL1A1* and *FN1* (refs. [1–3,5,6]). RT-qPCR results showed no statistically significant differences for these markers in *FOCAD*-knockout compared with WT isogenic LX-2 cells (Fig. 6b). Because of their immortalized state and continuous passaging in vitro, LX-2 cells are regarded to be in a semi-activated state, which can mask the extent of myofibroblast-like differentiation[34]. Despite that, LX-2 cells remain responsive to TGFβ1 (ref. [34])—a central profibrotic cytokine promoting HSC activation[1–3,6,36]. In a new experimental strategy, parental WT and isogenic *FOCAD*-knockout cells were incubated with TGFβ1 after serum starvation. RT-qPCR results indicated that both WT and *FOCAD*-null cells were responsive to TGFβ1 treatment, but there was no significant difference in the extent of the response between both genotypes (Fig. 6c). The apparent absence of a distinctive phenotype in *FOCAD*-null HSCs/myofibroblasts led us instead to examine the role of *FOCAD* in hepatocytes. RT-qPCR for a panel of curated markers related to hepatocyte function revealed a significant upregulation of *CK19* (refs. [37,38]), *LCN2* (refs. [39,40]) and *CHAC1* (refs. [41,42]) and downregulation of *ALB* (refs. [43,44]), *CYP3A4* (refs. [45,46]) and *LOX* (refs. [47,48]) in *FOCAD*-knockout cells relative to their WT isogenic human hTERT-immortalized hepatocytes (Fig. 6e). These data were reproducible and robust in polyclonal and monoclonal cell lines established for these tests. As a complementary approach, we also examined the secretome of these cells using a Luminex array. The data showed a clear separation between the WT and the *FOCAD*-null hepatocytes, with both the polyclonal and the monoclonal populations showing deviant cytokine secretion profiles (Fig. 6f). We detected 4 upregulated and 23 downregulated cytokines in the supernatant from both polyclonal and monoclonal populations (Fig. 6g). Among them, the top upregulated cytokines were CCL2 (a.k.a. MCP-1), IL-7 and MIF, whereas the top downregulated cytokines were CCL20 and TSLP (Fig. 6g), all of which are linked to liver damage and inflammation[49–54]. Altogether, our analyses of cultured human hepatocytes provide tangible

evidence that this cell type may represent the cell-of-origin of the liver phenotype detected in the patients bereft of FOCAD activity.

Discussion

In conclusion, we have characterized recessive loss-of-function mutations in *FOCAD* as the cause of a new Mendelian syndrome affecting children. This is supported by genetic and clinical data, an animal model of the disease and functional tests performed in vitro using patient-derived and disease-relevant human cell lines. We establish a causal, and heretofore unknown, link between *FOCAD* deficiency and neonatal liver cirrhosis. The expression levels of *FOCAD* are reported to be highest in the brain[11], and its loss of heterozygosity has been previously associated with the development of glioma[11,12] or colorectal cancer[13]. To date, no predispositions to neurological disorders or any form of cancer in the probands or their asymptomatic heterozygous relatives have been documented.

Our work adds to previous studies that have documented the existence of genetic networks safeguarding liver homeostasis[55,56] and highlights the importance of the SKI mRNA surveillance pathway in this process. Our functional data from *FOCAD*-deficient zebrafish and human knockout hepatocytes provides some insights into the function of FOCAD in relation to SKIC2. We find that the presence of FOCAD is essential to sustain the protein half-life of SKIC2 and SKIC3—two essential components of the SKI complex. The existence of additional SKI complex-associated proteins had been suggested previously by Lange et al.[25], who described how RST1 and RIPR connect the cytosolic RNA exosome to the SKI complex in *Arabidopsis*. Notably, both FOCAD and RST1 proteins contain a DUF3037, suggesting a role of this conserved domain in mediating protein interactions within the SKI complex.

Germline recessive mutations in *SKIC2* (MIM600478) and *SKIC3* (MIM614589) cause Mendelian disorders known as tricho-hepato-enteric syndrome (THES) type 1 (MIM614602) and type 2 (MIM222470), respectively, both of which present with frequent hepatic anomalies[57–60] (Table 1 and Extended Data Fig. 3). The most common liver defects in THES patients were also detected in our cohort of *FOCAD*-deficient children, including cirrhosis, cholestasis, hepatomegaly, elevated hepatic enzymes and iron overload (Table 1). Shared clinical manifestations between *FOCAD*-deficient and THES patients go beyond liver disease, with overlaps in terms of IUGR, diarrhea, cardiac and facial abnormalities, and coagulation defects[57–60] (Table 1 and Extended Data Fig. 3). However, hair abnormalities, skin defects and immune deficiency, while common in both types of THES, were unremarkable in *FOCAD*-deficient individuals (Table 1 and Extended Data Fig. 3). This partial clinical overlap and the realization that the proteins encoded by these genes form a molecular complex lends credence to the notion that the SKI pathway might be acutely required for liver homeostasis.

Our in vitro functional data on cultured HSCs and hepatocytes revealed that the latter are more sensitive to the loss of FOCAD activity, indicating that this could be the cell-of-origin responsible for liver cirrhosis in these diseased children. How a compromised SKI complex would acutely disrupt hepatocytes, but not dermal fibroblasts or HSCs, remains unclear

given that there is no paralog that could functionally compensate for its loss in other lineages. We can surmise that certain transcripts that are normally targeted for degradation by the SKI mRNA surveillance pathway may accumulate and become toxic to hepatocytes specifically. If these transcripts are coding, translational distress could ensue and lead to inflammatory and dysfunctional outcomes in *FOCAD*-null hepatocytes. Uncleared damaged or difficult-to-translate mRNAs could also induce ribosome stalling and collisions, which trigger a series of integrated stress responses[61,62]. Whichever these may be, our observation that *FOCAD*-deficient hepatocytes produce significantly less albumin, correlating with the hypoalbuminemia witnessed in *FOCAD*-deficient children, and overproduce CCL2—a key cytokine involved in hepatic inflammation[49]—seems to support the notion that these hepatocytes are injured and fail to fulfill their normal role. The increased secretion of CCL2, which acts as a potent activator of dormant HSCs[50], is expected to worsen the fibrogenic and inflammatory processes at play in *FOCAD*-mutant patients. Interestingly, circulating CCL2 has been proposed as a potential biomarker and negative prognostic readout for liver cirrhosis, since its levels correlate with disease severity in humans[63]. Furthermore, the inhibition of the CCL2/CCR2 signaling axis in mice was shown to diminish macrophage infiltration, ameliorate steatosis, reduce liver damage and suppress HCC incidence and tumor burden during chronic liver disease[64–66]. Our results add further evidence that this chemokine represents a potential therapeutic target for rare and common forms of liver disease. This provides a compelling rationale for further preclinical exploration of CCL2/CCR2 antagonism for the treatment of this pediatric form of cirrhosis driven by *FOCAD* deficiency, especially given the availability of small molecule inhibitors and neutralizing antibodies to this target[67].

Online content

Any methods, additional references, Nature Research reporting summaries, source data, extended data, supplementary information, acknowledgements, peer review information; details of author contributions and competing interests; and statements of data and code availability are available at https://doi.org/10.1038/s41588-022-01120-0.

Methods

Ethical approval

Written informed consent was obtained from all individuals (parents and patients from each family) for genetic testing, skin biopsies (patients F1-II:1 and F2-II:2 and two healthy unrelated individuals) and the use of the clinical information presented in this study, according to the ethical approval of the local IRB in India, France, the United States, Saudi Arabia, Pakistan, Portugal and Brazil. The study protocol was approved by A*STAR Institutional Review Board (2019-087) in Singapore.

Patient recruitment

The affected F1-II:1 patient was diagnosed by K.M.G. at the Kasturba Medical College in Manipal (India). The affected F2-II:2 patient was diagnosed by M.V. and B.C. at the Nantes University Hospital Center (France). The affected F3-II:1 patient was diagnosed by

A.L. at the Children's Hospital Colorado in Aurora (United States). The affected F4-II:1 patient was diagnosed by F.A.M. at the King Abdullah Specialized Children Hospital in Riyadh (Saudi Arabia). The affected F5-II:1, F5-II:2 and F5-II:3 patients were diagnosed by N.A.A.-S. at the John Hopkins Aramco Healthcare in Dhahran (Saudi Arabia). The affected F6-II:3, F6-II:4 and F6-II:6 patients were diagnosed by E.A.F. at the Children's Specialist Hospital, King Fahad Medical City in Riyadh (Saudi Arabia). The affected F7-II:3 patient was diagnosed by H.A.C. at the Children's Hospital and Institute of Child Health in Lahore (Pakistan). The affected F8-II:3 patient was diagnosed by J.D. at the Lisbon North University Hospital Center (Portugal). The affected F9-II:2 patient was diagnosed by L.R. and G.P. at the Sírio-Libanês Hospital in São Paulo (Brazil). The affected F10-II:2 patient was diagnosed by R.S. and E.C. at the Sírio-Libanês Hospital in Brasilia (Brazil).

Whole genome and exome sequencing

Trio whole genome sequencing and whole exome sequencing were performed at the different research institutes according to local standard procedures. Briefly, the Ion TargetSeq Exome Enrichment Kit (Life Technologies) was used for exome capture from 1 μg of high-quality genomic DNA from the probands (F1, F2, F4, F5, F6, F7, F8). The Ion One-Touch System (Life Technologies) was used for exosome library preparation and sequencing was performed on an Ion Proton instrument (Life Technologies) using one ION PI Chip. Trio rapid whole genome sequencing was performed as previously described[68] for F3, F9 and F10. Briefly, following DNA extraction from whole blood, sequencing libraries were constructed using the TruSeqDNA PCR-Free Library Prep Kit (Illumina) according to the manufacturer's instructions. Paired-end sequencing was performed on a NovaSeq 6000 and S1 flowcell (Illumina).

Sequence reads were aligned to the human reference genome (GRCh37/hg19 Assembly, UCSC Genome Browser; https://genome.ucsc.edu/) using the Torrent Mapping Alignment Program (TMAP) from the Torrent Suite (v.5.0.2) for whole exome sequencing and the DRAGEN processor (Illumina) for whole genome sequencing. The variants were called using the Torrent Variant Caller plugin (v.5.0.2), annotated with their associated gene, location, quality score and coverage, and analyzed and interpreted using the Clinical Reporter (Fabric Genomics). Following the addition of Human Phenotype Ontology terms, variants were filtered to retain those with allele frequencies of less than 0.5% in population databases including the 'common and no known medical impacts' database at NCBI (https://ftp.ncbi.nlm.nih.gov/pub/clinvar/vcf_GRCh37/), the Genome Aggregation Database (https://gnomad.broadinstitute.org/), the Exome Sequencing Project (http://evs.gs.washington.edu/EVS/), the UK10K database (https://www.uk10k.org/) and the BRAVO/TOPmed database (https://bravo.sph.umich.edu/freeze8/hg38/). Identified *FOCAD* genetic variants were confirmed orthogonally by Sanger sequencing using standard methods and chemicals (primer sequences available in Supplementary Table 8). In silico prediction of functional consequences was conducted using the open access software SIFT[69], Polyphen2 (ref. [70]), MutationTaster[71], CADD[72], DANN[73], GERP RS, PhyloP100way Vertebrate and Align-GVGD. Variants affecting splicing were predicted by MaxEntScan[74], NNSPLICE, GeneSplicer[75], Human Splicing Finder[26], BDGP and NetGene2. Finally, data curation was

performed to classify the *FOCAD* variants according to the guidelines of the American College of Medical Genetics and Genomics and the Association for Molecular Pathology[76].

Abdominal magnetic resonance imaging

Magnetic resonance imaging (MRI) of the liver was conducted using available clinical techniques at the centers caring for the subjects. Techniques included Eovist contrast injection and standard T1 and T2 weighted images, as well as volumetric analysis to quantify liver size.

Electron microscopy

For assessment of hepatic ultrastructural features in patient F3-II:1, a portion of the liver tissue collected via needle biopsy was processed according to standard electron microscopy procedures. Briefly, tissue was fixed in 2.5% buffer glutaraldehyde (BCC Biochemical), postfixed in 1% osmium tetroxide, dehydrated through a graded alcohol series and embedded into Epon epoxy resin. Semithin survey sections (~500 nm) were collected and stained with Azure Blue for light microscopy. Ultrathin sections (~100 nm) were collected, poststained with uranyl acetate and lead citrate before examination using a JSM-1400plus TEM (JEOL Ltd) equipped with a Gatan Model 832 digital camera. Eight sections from different regions of the specimen were analyzed, and representative images are shown in the figures.

Cell culture

Primary dermal fibroblast cultures were established from skin biopsies from patients F1-II:1 and F2-II:2 and two unaffected and unrelated individuals (WT1 and WT2), following standard procedures[77]. Primary dermal fibroblast cell lines, HEK293T cells (ATCC, catalog no. CRL-3216, RRID:CVCL_0063) and LX-2 cells (Millipore, catalog no. SCC064, RRID: CVCL_5792, gift from H. Weiping (Duke-NUS Medical School, Singapore)) were cultured in complete High Glucose Dulbecco's Modified Eagle Medium (HyClone) supplemented with 10% fetal bovine serum (FBS) (Biological Industries) and 2 mM L-glutamine (Biological Industries). Hc3716-hTERT cells (a gift from P. Kaldis (Institute of Molecular and Cell Biology, A*STAR, Singapore)) were cultured in HCM Hepatocyte Culture Medium BulletKit (Lonza, catalog no. CC-3198) supplemented with 5% FBS and 10% human serum (Sigma-Aldrich, catalog no. H4522). All cell lines were maintained in a humidified atmosphere at 5% CO_2 and 37 °C and tested negative for mycoplasm using the MycoAlert Mycoplasma Detection Kit (Lonza, catalog no. LT07-118).

Generation of CRISPR-mediated *FOCAD*-knockout cell lines

FOCAD-knockout LX-2 and Hc3716-hTERT cell lines were generated using the CRISPR-Cas9 genome editing technology. A pair of single-guide RNAs (sgRNAs) was used to simultaneously target exons 5 and 6 of the human *FOCAD* gene (Supplementary Table 6). The sgRNAs sequences were cloned into the lentiCRISPRv2 vector (a gift from F. Zhong (Nanyang Technological University, Singapore)). Lentiviruses were produced in HEK293T cells by cotransfection of third-generation helper plasmids using Lipofectamine 2000 (Invitrogen, catalog no. 11668019), according to the manufacturer's protocol. Lentiviruses

Europe PMC Funders Author Manuscripts

were harvested for 3 consecutive days, concentrated using Lenti-X Concentrator (Takara, catalog no. 631231) and stored at −80 °C until use. Parental cells were infected in complete media supplemented with 5 μg ml^{-1} polybrene and subsequently selected for 14 days with 2 μg ml^{-1} puromycin (LX-2) or 400 μg ml^{-1} neomycin (Hc3716-hTERT). Clones were obtained from the polyclonal populations by serial dilution.

Transient transfections

The pcDNA3.1-MYC-FOCAD expression plasmid was a gift from R. Weber (Hannover Medical School, Germany). Transient transfection in HEK293T cells was performed using the FuGENE 6 Transfection Reagent (Promega, catalog no. E2691) at a 1:3 (DNA:transfection reagent) ratio in Opti-MEM medium (Gibco, catalog no. 31985062), according to the manufacturer's protocol.

Immunofluorescence staining

HEK293T cells were plated into Millicell EZ 4-well glass slides (Millipore, catalog no. PEZGS0416), previously coated with poly-L-lysine (Sigma-Aldrich, catalog no. P4707). At 48 h after transfection, cells were fixed in 4% paraformaldehyde for 10 min at room temperature and subsequently permeabilized with 0.2% Triton X-100 in PBS for 10 min at room temperature. Cells were blocked with 5% BSA in PBS for 1 h at room temperature and subsequently incubated with the primary antibody overnight at 4 °C (Supplementary Table 7). After three washes with PBS, secondary antibody labelled with Alexa Fluor 488 dye (Invitrogen, catalog no. A-21200, 1:1,000) was incubated for 1 h at room temperature in the dark. Three washes with PBS were performed before staining nuclei with 1 μg ml^{-1} 4,6-diamidino-2-phenylindole (DAPI) for 5 min at room temperature. Slides were mounted in ProLong Diamond Antifade Mountant (Invitrogen, catalog no. P36961). Images were taken with an Olympus FV1000 upright confocal microscope. Similar results were obtained in three independent experiments, and representative images are shown in the figures.

RNA extraction and RT-qPCR

Total RNA from cells, zebrafish livers and zebrafish embryos was extracted using the RNeasy Mini Kit (Qiagen, catalog no. 74104) following the manufacturer's protocol, including the optional DNase RNase-free treatment. All biological samples were homogenized using QIAshredder (Qiagen, catalog no. 79654) before RNA extraction. Zebrafish livers and embryos were first disrupted using a syringe and a 23G needle. A total of 30 zebrafish embryos were collected as a sample for each analyzed developmental stage. A 1 μg sample of the extracted RNA was converted to complementary DNA using the Iscript Reverse Transcription Supermix (Bio-Rad, catalog no. 1708840) according to the manufacturer's instructions. RT-qPCR reactions were carried out using the Power SYBR Green PCR Master Mix (Applied Biosystems, catalog no. 4309155) and specific primers for the target genes (Supplementary Table 8) on the 7900HT Fast Real-Time PCR System (Applied Biosystems). RT-qPCR assays involved three biological replicates per condition and three technical replicates per sample. *GAPDH* was used as the housekeeping gene to normalize gene expression. GraphPad Prism v.9 was used to statistically analyze the data.

FOCAD custom-made antibody generation and blot-affinity purification

A custom-made rabbit polyclonal antibody was raised against the C terminus of human FOCAD (EFKKKAVWTRAYGW-COOH). The high conservation of the antigen sequence across orthologs makes the antibody suitable to efficiently detect FOCAD protein in humans and zebrafish. The antibody was produced and affinity-purified by GL Biochem. To optimize the antibody for western blot applications, antisera was affinity-purified over polyvinylidene difluoride (PVDF) blots as described[78]. Briefly, HEK293T cells were transfected with the pcDNA3.1-MYC-FOCAD plasmid (as described above). The resulting overexpressed human FOCAD protein was separated by SDS–PAGE and transferred to a PVDF membrane. After blocking with 5% milk in TBST (50 mM Tris-HCl pH 7.5, 150 mM NaCl, 0.05% Tween-20) for 30 min, antisera (50 μg ml^{-1} diluted in 0.1% BSA in TBST) was incubated to blot strips overnight at room temperature. Bound antibodies were washed three times for 5 min each with TBST, eluted on ice for 3 min with 2 ml of glycine elution buffer (0.1 M glycine, 0.5 M NaCl, 0.05% Tween-20, pH 2.8) and immediately neutralized with 0.3 ml of 1 M Tris buffer pH 8.1. For probing western blots, undiluted blot-affinity-purified anti-FOCAD was used (Supplementary Table 7).

Protein isolation and analysis

For total protein extraction, cells were lysed by scraping using appropriate amount of ice-cold RIPA buffer (50 mM Tris-HCl pH 7.5, 150 mM NaCl, 1% NP-40, 1% Na-deoxycholate) supplemented with a Protease Inhibitor Cocktail (Sigma-Aldrich, catalog no. P2714). Lysates were centrifuged at 17,000*g* and 4 °C for 10 min to remove cell debris, and the supernatants were collected. Cytosolic, membrane and nuclear protein extracts were obtained using the Cell Fractionation Kit Standard (Abcam, catalog no. ab109719), according to the manufacturer's instructions. Protein quantification was performed using the Pierce BCA Protein Assay Kit (Thermo Fisher Scientific, catalog no. 23225). For western blotting, samples were reduced in Laemmli loading buffer containing dithiothreitol and denatured at 95 °C for 5 min. Protein samples and the Precision Plus Protein Dual Color Standard (Bio-Rad, catalog no. 1610374) were loaded into 4–20% Criterion TGX Precast Midi Protein Gels (Bio-Rad, catalog no. 5671093) in 1× running buffer (25 mM Tris, 200 mM Glycine, 0.1% SDS) and run at 120 V until desired separation. Proteins were transferred from the polyacrylamide gel to a 0.2 μm Immun-Blot® Low Fluorescence PVDF Membrane (Bio-Rad, catalog no. 1620261) using the Trans-Blot Turbo Transfer System (Bio-Rad) for 7 min. Membranes were blocked for 1 h at room temperature with 5% milk or 5% BSA in TBST, and then incubated with the primary antibody overnight at 4 °C (Supplementary Table 7). After several washes in TBST, membranes were incubated for 1 h at room temperature with the respective HRP-conjugated secondary antibody (anti-mouse, catalog no. 715035150 or anti-rabbit, catalog no. 711035152, 1:4,000, Jackson ImmunoResearch) in 5% milk or 5% BSA in TBST. After several washes in TBST, the signal was revealed with the SuperSignal West Chemiluminescent Substrate System (Thermo Fisher Scientific, catalog no. 34080/34076/34096) for 1 min at room temperature. Membranes were then exposed to CL-Xposure Films (Thermo Fisher Scientific, catalog no. 34091) and developed by a Carestream Kodak developer. Western blot assays involved at least three independent experiments, and representative images are shown in the figures.

Luminex cytokine array

Hc3716-hTERT cells were seeded at 50% confluency in six-well plates with 2 ml medium. After 3 days in culture, 1 ml supernatant was harvested per well and submitted for Luminex analysis using the ProcartaPlex, Human Customized 65-plex Panel (Thermo Fisher Scientific, catalog no. EPX650-10065-90) to measure the following targets: APRIL, BAFF, BLC, CD30, CD40L, ENA-78, Eotaxin, Eotaxin-2, Eotaxin-3, FGF2, Fractalkine, G-CSF, GM-CSF, Gro-α, HGF, I-TAC, IFN-α, IFN-γ, IL-10, IL-12p70, IL-13, IL-15, IL-16, IL-17A, IL-18, IL-1α, IL-1β, IL-2, IL-20, IL-21, IL-22, IL-23, IL-27, IL-2R, IL-3, IL-31, IL-4, IL-5, IL-6, IL-7, IL-8, IL-9, IP-10, I-TAC, LIF, CCL2, CCL3, CCL4, CCL7, CCL8, CCL20, M-CSF, MDC, MIF, MIG, MMP1, bNGF, SCF, SDF-1α, TNF-α, TNF-β, TNF-R2, TRAIL, TSLP, TWEAK and VEGF-A.

Briefly, harvested supernatants and standards were incubated with fluorescent-coded magnetic beads precoated with respective antibodies in a black 96-well clear-bottom plate overnight at 4 °C. After incubation, plates were washed five times with wash buffer (1% BSA, 0.05% Tween-20 in PBS). Sample–antibody–bead complexes were incubated with biotinylated detection antibodies for 1 h, and subsequently washed five times with wash buffer. Streptavidin-phycoerythrin was then added and incubated for 30 min. After washing the plates again five times, sample–antibody–bead complexes were resuspended in sheath fluid for acquisition on the FLEXMAP 3D (Luminex) using the xPONENT v.4.0 (Luminex) software. Data were analyzed using Bio-Plex Manager v.6.1.1 (Bio-Rad). Standard curves were generated with a five-parameter logistic algorithm, reporting values for both mean fluorescence intensity and concentration data.

Zebrafish husbandry

We performed zebrafish husbandry procedures in compliance with the Singapore National Advisory Committee on Laboratory Animal Research Guidelines from the Institutional Animal Care and Use Committee (A*STAR Biological Resource Centre, IACUC 161172). Zebrafish embryos were raised at 28.5 °C in egg water (5 mM NaCl, 0.17 mM KCl, 0.33 mM $CaCl_2$, 0.33 mM $MgSO_4$).

CRISPR-mediated *focad* knockout in zebrafish

Zebrafish *focad* mutant lines were generated using the CRISPR-Cas9 genome editing technology as previously described[79]. Briefly, a custom gBLOCK (Integrated DNA Technologies) was designed incorporating a sgRNA-targeting sequence preceded by a T7 promoter sequence. The sgRNA targeted a sequence on exon 4 of the *focad* gene (Supplementary Table 6). It was synthesized using the MEGAshortscript T7 Transcription Kit (Invitrogen, catalog no. AM1354) following the manufacturer's instructions and purified using the RNeasy Mini Kit (Qiagen, catalog no. 74104). Cas9 mRNAs were synthesized using the mMESSAGE mMACHINE SP6 Transcription Kit (Thermo Fisher Scientific, catalog no. AM1340) from a *Not*I-linearized zebrafish codon-optimized Cas9 construct in pCS2+ (a gift from T. Carney (Nanyang Technological University, Singapore)). The sgRNA and Cas9 mRNAs were mixed together to a concentration of 250 ng μl^{-1} each, and 2 nl of this solution was injected into the yolk of 1-cell AB zebrafish embryos. *focad*$^{\Delta 7}$ mutants

were genotyped by sequencing a 737 bp PCR product containing *focad* exon 4, amplified with specific primers (Supplementary Table 8).

Histological analysis

Adult 3-month-old male zebrafish were euthanized by hypothermic shock. Gastrointestinal organs were harvested, fixed in 4% paraformaldehyde for 48 h at 4 °C, dehydrated in 70% ethanol for 48 h at 4 °C and eventually embedded in paraffin. Sections (5 µm thick) were cut, and those containing liver tissue were selected. Liver biopsies from patients F1-II:1 and F2-II:2 followed a similar processing. We performed H&E, reticulin, periodic acid Schiff (PAS), PAS-diastase (PAS-D), Gordon and Sweet's, pricosirius red and Masson's trichrome stainings following standard procedures. Brightfield images were obtained using a Zeiss Axioimager Z1 upright microscope. Terminal deoxynucleotidyl transferase dUTP nick end labelling (TUNEL) staining on zebrafish liver sections was performed using the In Situ Cell Death Detection Kit (Roche, catalog no. 11684795910), following the manufacturer's protocol. Fluorescent images were taken with an Olympus FV3000 inverted confocal microscope. Quantifications of TUNEL+ cells were performed on six randomly selected images per liver.

Histological analysis of liver biopsies from patients involved a minimum of three sections from different regions of the specimen. Similar histological results were obtained for all the sections from the same biopsy, and representative images are shown in the figures. Histological analysis of zebrafish livers involved at least two sections from different regions of the same liver from a minimum of three animals per genotype. Similar histological results were obtained for samples from the same genotype, and representative images are shown in the figures.

RNA-seq and analysis

Liver RNA samples from male adult zebrafish (3 months old) were prepared as explained above and submitted to Omics Drive (Singapore) for RNA-sequencing analysis. Briefly, 1 µg total RNA with a RNA integrity number value above 6.5 was used from each sample for next-generation sequencing library preparation. We performed poly(A) mRNA isolation, fragmentation and priming using the NEBNext Poly(A) mRNA Magnetic Isolation Module Kit (New England Biolabs, catalog no. E7490S), following the manufacturer's protocol. First-strand cDNA was synthesized using ProtoScript II Reverse Transcriptase (New England Biolabs, catalog no. M0368S), and the second cDNA strand was synthesized using the Second Strand Synthesis Enzyme Mix (New England Biolabs, catalog no. E6114). The double-stranded cDNAs were purified using beads and subsequently treated with the NEBNext End Prep Enzyme Mix (New England Biolabs, catalog no. E6050S) for dA-tailing. Then, adapters were added at both strand ends by TA ligation and adapter-ligated cDNAs were size selected using beads, recovering fragments of 420 bp (with an approximate insert size of 300 bp). Each sample was then amplified by PCR for 13 cycles using P5 and P7 primers, with both primers carrying sequences that make them suitable to perform bridge PCR and the P7 primer carrying a six-base index allowing multiplexing. The PCR products were cleaned up using beads, validated using a Qsep 100DNA analyzer (BiOptic) and quantified using the Qubit v.3.0 Fluorometer (Invitrogen). Libraries with

different indices were multiplexed and loaded on an HiSeq/NovaSeq instrument (Illumina) according to the manufacturer's indications. Sequencing was carried out using a 2 × 150-bp paired-end configuration. Image analysis and base calling were conducted by the HiSeq/NovaSeq Control Software v.1.7.5 (Illumina).

Paired-end clean reads were aligned to the reference genome (GRCz11 Assembly, UCSC Genome browser) using TopHat v.2.0.12. To quantify gene expression levels, HTSeq v.0.6.1 was used to count the reads numbers mapped to each gene and to calculate the fragments per kilobase millions data. Differential expression analysis was performed using the DESeq R package (v.1.18.0). The resulting P values were adjusted (P_{adj}) using Benjamini and Hochberg's approach. Genes with $\log_2$(fold change) greater than 3 or less than –3 and $-\log_{10}(P_{adj})$ greater than 2.5 were considered statistically significantly dysregulated. Dysregulated GO terms were identified using the GO database (http://geneontology.org/) and the over-represented P values were calculated with the hypergeometric statistical test. Dysregulated KEGG pathways were identified using the KEGG pathway database (https://www.genome.jp/kegg/pathway.html), and the Q values were calculated using the hypergeometric statistical test and Benjamini and Hochberg's approach for correction.

Glycerophospholipids analysis

Liver samples were extracted with 500 µl methanol containing 10 nM of internal standards (C17:0 or C17:1) in 2-ml CKmix tubes (Precellys, Bertin Instruments), homogenized at 4,000g and < 8 °C and centrifuged at 5,700g and 4 °C. The supernatant was collected and evaporated to dryness overnight before being resuspended in methanol for liquid chromatography-mass spectrometry analysis. Methanol extracts were analyzed using a targeted lipidomics method with modifications from Bligh et al.[80] on a Waters Xevo TQ-XS triple quadrupole mass spectrometer with both positive and negative electrospray ionization detection modes and ACQUITY UPLC BEH C18 column (2.1 × 100 mm, 1.7 µm). Mobile phases A and B were water and methanol with 5 mM ammonium acetate plus 0.01% formic acid, respectively. An isocratic elution was used with 2% A and 98% B. Column temperature was 45 °C, flow rate was 0.4 ml min^{-1} and injection volume was 5 µl.

A total of 98 glycerophospholipids were quantified, and probabilistic quotient normalization was applied to the data before multivariate data analysis. OPLS-DA was applied to the data (SIMCA-P v.15, Umetrics AB). The model comparing data obtained from *WT* and *MZ focad*$^{\Delta 7/\Delta 7}$ zebrafish livers was validated by permutation test and CV-ANOVA ($P < 0.05$). The correlation coefficients were considered as significant when higher than 0.5 ($P < 0.05$).

Reporting summary

Further information on research design is available in the Nature Research Reporting Summary linked to this article.

Extended Data

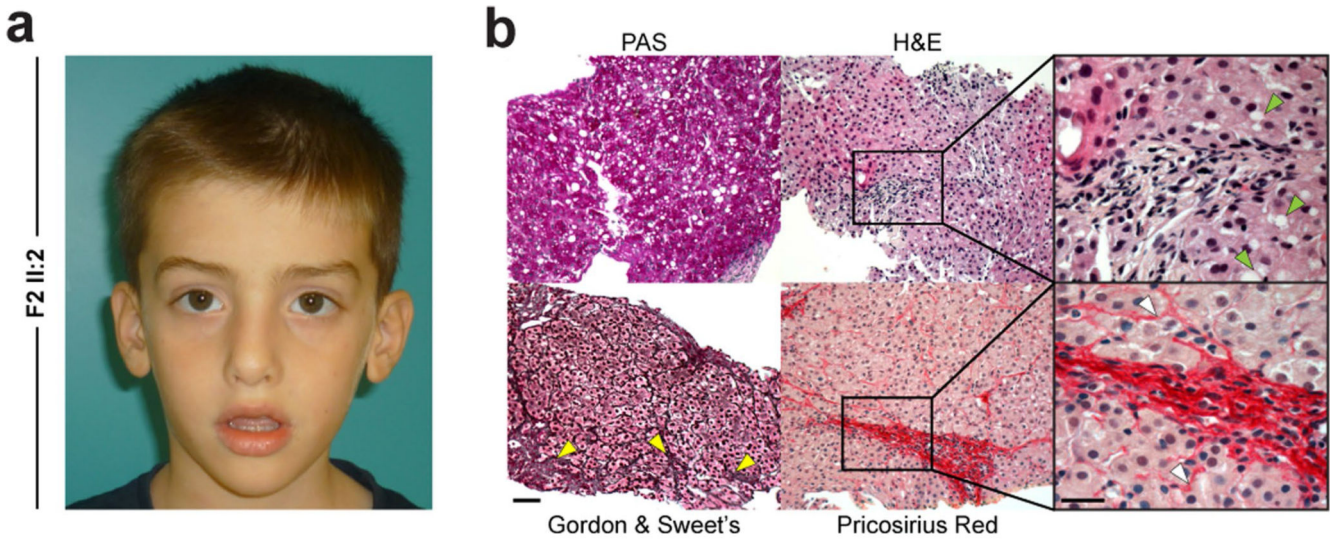

Extended Data Fig. 1. Clinical data from patient F2-II:2 (France).

a, Photograph of the patient showing a triangular face, high forehead and plagiocephaly. **b**, Liver biopsy at 2 years and 4 months. Periodic acid Schiff staining (PAS, top left) showed elevated intrahepatocellular glycogen. Gordon and Sweet's silver staining (bottom left) revealed some regions of the liver parenchyma with an abnormal reticular fiber pattern (yellow arrows). H&E staining (top middle and right) showed presence of fibrogenic connective tissue (black frame) and lipid vesicles in hepatocytes indicative of steatosis (green arrows). Picrosirius red staining (bottom middle and right) confirmed the presence of fibrotic bands (black frame) and highlighted the presence of pericellular collagen fibers among hepatocytes (white arrows). Scale bars, 50 μm (bottom left) and 25 μm (bottom right).

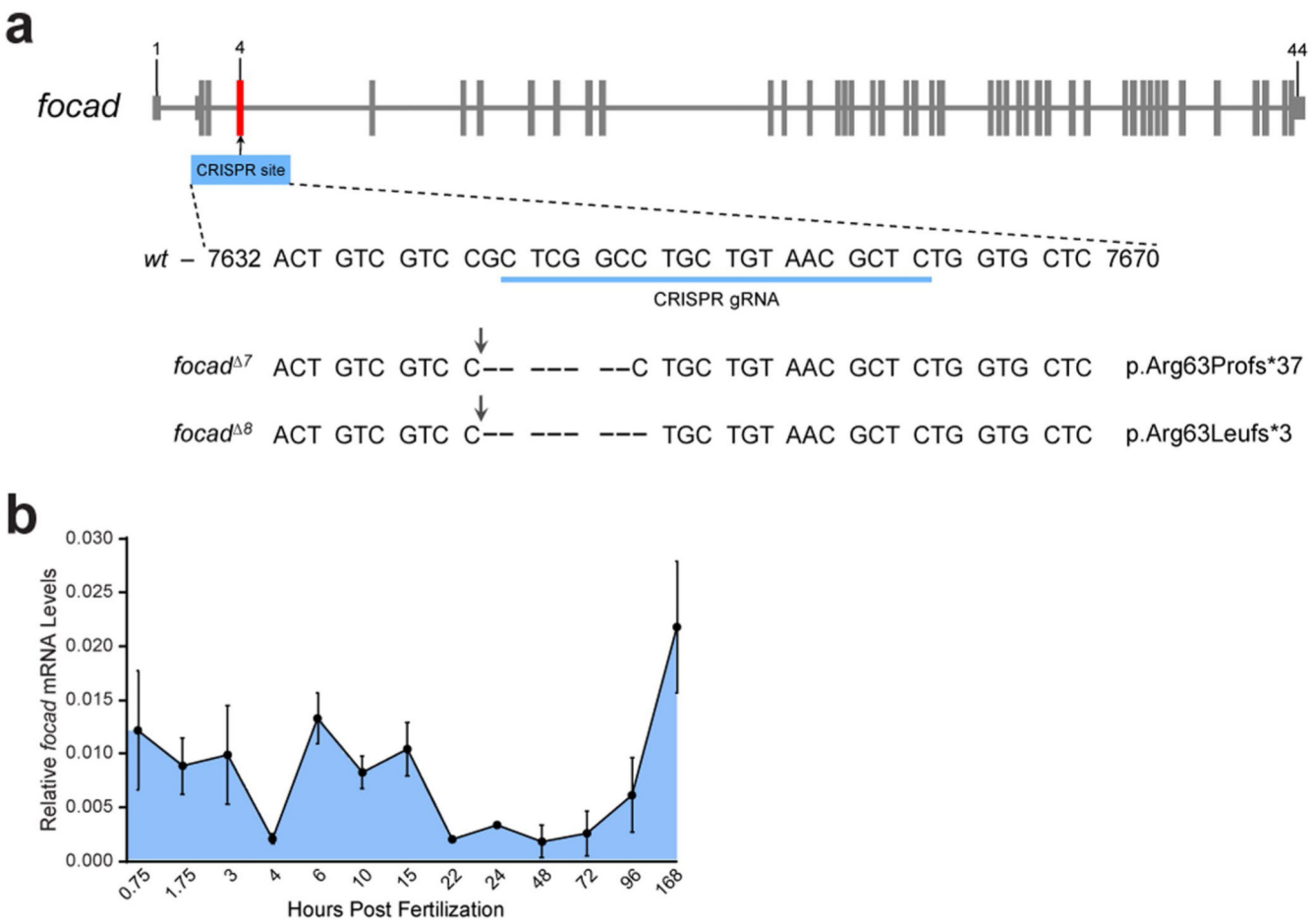

Extended Data Fig. 2. *focad* is maternally contributed in zebrafish.

a, Schematic diagram of the genomic structure of *focad* in zebrafish. Two germline deletion mutations were selected to generate *focad* knockouts using CRISPR-Cas9 technology. The *focad* gene comprises 44 exons (bars). The blue line highlights the region targeted by the CRISPR guide RNA (gRNA) in exon 4. Black arrows point where the genomic deletions of 7 (*focad*$^{\Delta 7}$) and 8 (*focad*$^{\Delta 8}$) base pairs have occurred, which result in out-of-frame alleles creating early stop codons. **b**, Temporal RT-qPCR quantification of the expression levels of *focad* relative to *β-actin* during the 7 days postfertilization. *focad* is maternally contributed to the egg. Data are presented as mean ± s.e.m. (n = 2 biological replicates of 30 to 50 embryos).

Europe PMC Funders Author Manuscripts

Europe PMC Funders Author Manuscripts

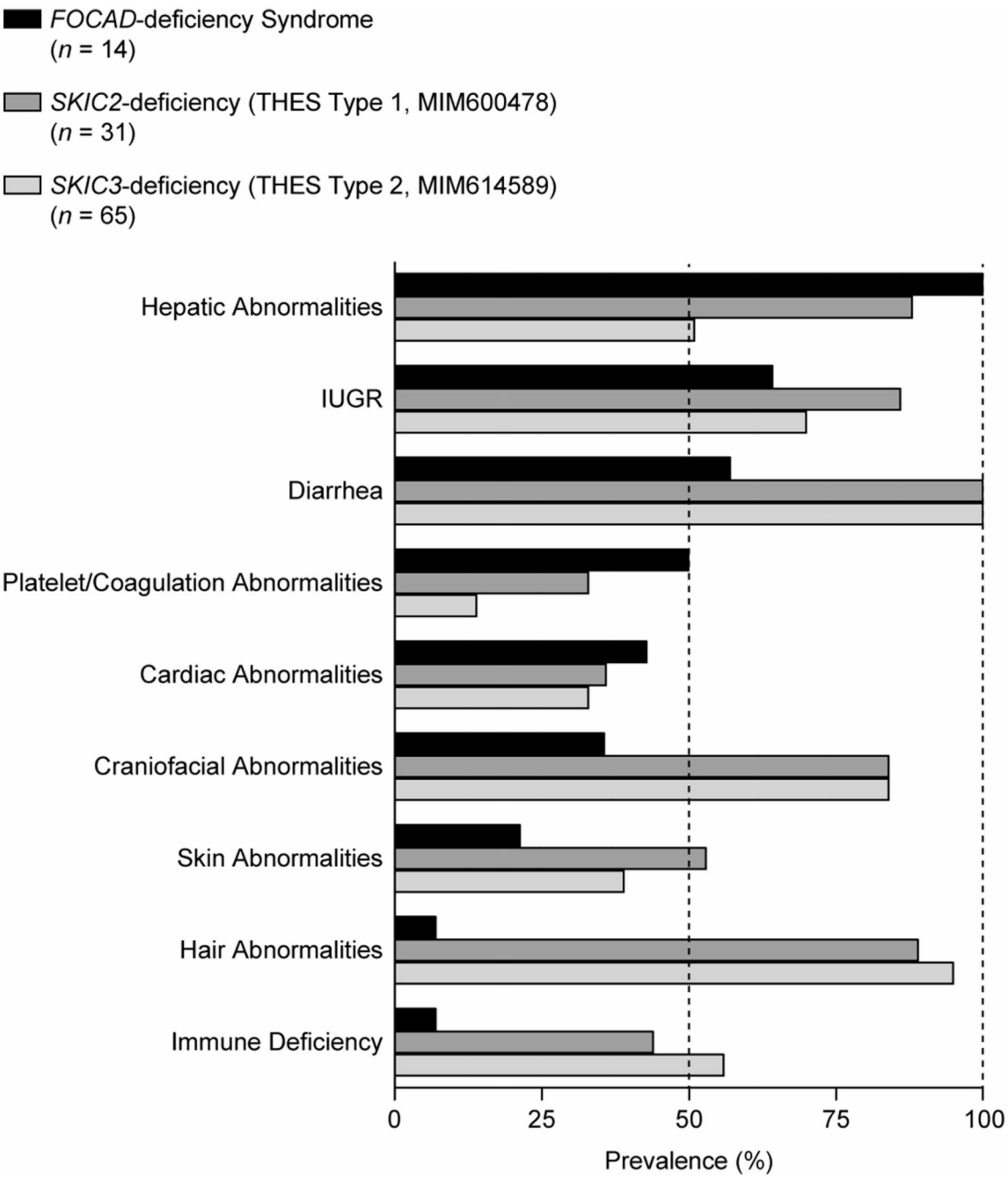

Extended Data Fig. 3. Overlap of the main clinical manifestations seen in *FOCAD*-deficient patients and THES type 1 and type 2.

Data related to both types of THES were extracted from Bourgeois et al.[57].

Supplementary Material

Refer to Web version on PubMed Central for supplementary material.

Acknowledgements

We are grateful to the families of affected individuals for their participation and kind cooperation in this study. We are also grateful to all members of the Reversade laboratory for constructive discussions and suggestions. We thank R. Weber (Hannover Medical School, Germany) for providing the FOCAD expression construct used for our transient transfections, as well as A. van Hoof (University of Texas Health Science Center at Houston, Texas, USA) and J. Mendell (University of Texas Southwestern Medical Center, Texas, USA) for their insights on the biology of the SKI complex. M.M. was supported by a Career Development Award (CDF Project NR C210812055) from the A*STAR, Biomedical Research Council (Singapore). K.M.G. was supported by the Clinical Research Center grant (IA/CRC/20/1/600002) from India Alliance (India). The authors also thank the King Fahad Medical City Research Center (Saudi Arabia) for the partial support to E.A.F. (grant no. 019-052). B.R. is a fellow of the Branco Weiss Foundation (Switzerland) and the National Research Foundation (Singapore), and an A*STAR and EMBO Young Investigator. This work was also supported by an inaugural Use-Inspired Basic Research (UIBR) central fund and a Brain-Body Initiative (BBI) grant in Neurometabolism to B.R. from the Agency for Science, Technology and Research (A*STAR) in Singapore.

Data availability

RNA-seq data and processed results have been deposited in the National Center for Biotechnology Information Gene Expression Omnibus public repository under accession number GSE168961. Source data are provided with this paper.

Code availability

No custom code was used for data analysis. All software and packages used are listed in the Methods section.

References

1. Elpek GÖ. Cellular and molecular mechanisms in the pathogenesis of liver fibrosis: an update. World J Gastroenterol. 2014; 20: 7260–7276.
2. Seki E, Brenner DA. Recent advancement of molecular mechanisms of liver fibrosis. J Hepatobiliary Pancreat Sci. 2015; 22: 512–518. [PubMed: 25869468]
3. Friedman SL. Hepatic fibrosis—overview. Toxicology. 2008; 254: 120–129. [PubMed: 18662740]
4. Ding B-S, et al. Divergent angiocrine signals from vascular niche balance liver regeneration and fibrosis. Nature. 2014; 505: 97–102.
5. Mederacke I, et al. Fate tracing reveals hepatic stellate cells as dominant contributors to liver fibrosis independent of its aetiology. Nat Commun. 2013; 4: 2823. [PubMed: 24264436]
6. Wynn TA, Ramalingam TR. Mechanisms of fibrosis: therapeutic translation for fibrotic disease. Nat Med. 2012; 18: 1028–1040. [PubMed: 22772564]
7. Schuppan D, Afdhal NH. Liver cirrhosis. Lancet. 2008; 371: 838–851. [PubMed: 18328931]
8. Mokdad AA, et al. Liver cirrhosis mortality in l87 countries between l980 and 20l0: a systematic analysis. BMC Med. 2014; 12: 145. [PubMed: 25242656]
9. Asrani SK, Devarbhavi H, Eaton J, Kamath PS. Burden of liver diseases in the world. J Hepatol. 2019; 70: 151–171. [PubMed: 30266282]
10. Yoshiji H, et al. Evidence-based clinical practice guidelines for liver cirrhosis 2020. Hepatol Res. 2021; 51: 725–749. [PubMed: 34228859]
11. Brockschmidt A, et al. KIAAl797/FOCAD encodes a novel focal adhesion protein with tumour suppressor function in gliomas. Brain. 2012; 135: 1027–1041. [PubMed: 22427331]
12. Brand F, et al. FOCAD loss impacts microtubule assembly, G2/M progression and patient survival in astrocytic gliomas. Acta Neuropathol. 2020; 139: 175–192. [PubMed: 31473790]
13. Weren RDA, et al. Germline deletions in the tumour suppressor gene FOCAD are associated with polyposis and colorectal cancer development. J Pathol. 2015; 236: 155–164. [PubMed: 25712196]

14. Wiech T, et al. Genome-wide analysis of genetic alterations in Barrett's adenocarcinoma using single nucleotide polymorphism arrays. Lab Invest. 2009; 89: 385–397. [PubMed: 18663352]
15. Toh-E A, Guerry P, Wickner RB. Chromosomal superkiller mutants of *Saccharomyces cerevisiae*. J Bacteriol. 1978; 136: 1002–1007. [PubMed: 363683]
16. Brown JT, Bai X, Johnson AW. The yeast antiviral proteins Ski2p, Ski3p, and Ski8p exist as a complex in vivo. RNA. 2000; 6: 449–457. [PubMed: 10744028]
17. Widner WR, Wickner RB. Evidence that the SKI antiviral system of *Saccharomyces cerevisiae* acts by blocking expression of viral mRNA. Mol Cell Biol. 1993; 13: 4331–4341. [PubMed: 8321235]
18. Synowsky SA, Heck AJR. The yeast Ski complex is a hetero-tetramer. Protein Sci. 2008; 17: 119–125. [PubMed: 18042677]
19. Halbach F, Reichelt P, Rode M, Conti E. The yeast Ski complex: crystal structure and RNA channeling to the exosome complex. Cell. 2013; 154: 814–826. [PubMed: 23953113]
20. Anderson JS, Parker RP. The 3' to 5' degradation of yeast mRNAs is a general mechanism for mRNA turnover that requires the SKI2 DEVH box protein and 3' to 5' exonucleases of the exosome complex. EMBO J. 1998; 17: 1497–1506. [PubMed: 9482746]
21. Tuck AC, et al. Mammalian RNA decay pathways are highly specialized and widely linked to translation. Molecular Cell. 2020; 77: 1222–1236. e13 [PubMed: 32048998]
22. Lee WS, Sokol RJ. Mitochondrial hepatopathies: advances in genetics and pathogenesis. Hepatology. 2007; 45: 1555–1565. [PubMed: 17538929]
23. Fabris L, et al. Pathobiology of inherited biliary diseases: a roadmap to understand acquired liver diseases. Nat Rev Gastroenterol Hepatol. 2019; 16: 497–511. [PubMed: 31165788]
24. Ozen H. Glycogen storage diseases: new perspectives. World J Gastroenterol. 2007; 13: 2541–2553. [PubMed: 17552001]
25. Lange H, et al. RST1 and RIPR connect the cytosolic RNA exosome to the Ski complex in Arabidopsis. Nat Commun. 2019; 10: 3871. [PubMed: 31455787]
26. Desmet F-O, et al. Human Splicing Finder: an online bioinformatics tool to predict splicing signals. Nucleic Acids Res. 2009; 37: e67. [PubMed: 19339519]
27. Jumper J, et al. Highly accurate protein structure prediction with AlphaFold. Nature. 2021; 596: 583–589. [PubMed: 34265844]
28. Schwabe RF, Maher JJ. Lipids in liver disease: looking beyond steatosis. Gastroenterology. 2012; 142: 8–11.
29. Ding H, Wang J, Ren H, Shi X. Lipometabolism and glycometabolism in liver diseases. BioMed Res Int. 2018; 2018 1287127
30. Uhlar CM, Whitehead AS. Serum amyloid A, the major vertebrate acute-phase reactant. Eur J Biochem. 1999; 265: 501–523. [PubMed: 10504381]
31. Aly HH, et al. RNA exosome complex regulates stability of the hepatitis B virus X-mRNA transcript in a non-stop-mediated (NSD) RNA quality control mechanism. J Biol Chem. 2016; 291: 15958–15974.
32. Zhu B, et al. The human PAF complex coordinates transcription with events downstream of RNA synthesis. Genes Dev. 2005; 19: 1668–1673.
33. Qu X, et al. The human DEVH-box protein Ski2w from the HLA is localized in nucleoli and ribosomes. Nucleic Acids Res. 1998; 26: 4068–4077.
34. Xu L, et al. Human hepatic stellate cell lines, LX-1 and LX-2: new tools for analysis of hepatic fibrosis. Gut. 2005; 54: 142–151. [PubMed: 15591520]
35. Waki K, et al. Establishment of functional telomerase immortalized human hepatocytes and a hepatic stellate cell line for telomere-targeting anticancer drug development. Cancer Sci. 2010; 101: 1678–1685.
36. Border WA, Noble NA. Transforming growth factor beta in tissue fibrosis. N Engl J Med. 1994; 331: 1286–1292. [PubMed: 7935686]
37. Junge N, Sharma AD, Ott M. About cytokeratin 19 and the drivers of liver regeneration. J Hepatol. 2018; 68: 5–7.
38. Yoneda N, et al. Epidermal growth factor induces cytokeratin 19 expression accompanied by increased growth abilities in human hepatocellular carcinoma. Lab Invest. 2011; 91: 262–272.

39. Chen J, et al. Hepatic lipocalin 2 promotes liver fibrosis and portal hypertension. Sci Rep. 2020; 10 15558 [PubMed: 32968110]
40. Xu Y, et al. Lipocalin-2 protects against diet-induced nonalcoholic fatty liver disease by targeting hepatocytes. Hepatol Commun. 2019; 3: 763–775. [PubMed: 31168511]
41. Mungrue IN, Pagnon J, Kohannim O, Gargalovic PS, Lusis AJ. CHAC1/MGC4504 is a novel proapoptotic component of the unfolded protein response, downstream of the ATF4-ATF3-CHOP cascade. J Immunol. 2009; 182: 466–476. [PubMed: 19109178]
42. Magne L, et al. ATF4 and the integrated stress response are induced by ethanol and cytochrome P450 2E1 in human hepatocytes. J Hepatol. 2011; 54: 729–737.
43. Henriksen JH, et al. Dynamics of albumin in plasma and ascitic fluid in patients with cirrhosis. J Hepatol. 2001; 34: 53–60. [PubMed: 11211908]
44. Feldmann G, Penaud-Laurencin J, Crassous J, Benhamou JP. Albumin synthesis by human liver cells: its morphological demonstration. Gastroenterology. 1972; 63: 1036–1048. [PubMed: 4565256]
45. Boon R, et al. Amino acid levels determine metabolism and CYP450 function of hepatocytes and hepatoma cell lines. Nat Commun. 2020; 11: 1393. [PubMed: 32170132]
46. Villeneuve J-P, Pichette V. Cytochrome P450 and liver diseases. Curr Drug Metab. 2004; 5: 273–282. [PubMed: 15180496]
47. Siegel RC, Chen KH, Greenspan JS, Aguiar JM. Biochemical and immunochemical study of lysyl oxidase in experimental hepatic fibrosis in the rat. Proc Natl Acad Sci USA. 1978; 75: 2945–2949. [PubMed: 26918]
48. Vadasz Z, et al. Abnormal deposition of collagen around hepatocytes in Wilson's disease is associated with hepatocyte specific expression of lysyl oxidase and lysyl oxidase like protein-2. J Hepatol. 2005; 43: 499–507. [PubMed: 16023247]
49. Mandrekar P, Ambade A, Lim A, Szabo G, Catalano D. An essential role for monocyte chemoattractant protein-1 in alcoholic liver injury: regulation of proinflammatory cytokines and hepatic steatosis in mice. Hepatology. 2011; 54: 2185–2197. [PubMed: 21826694]
50. Kobayashi K, et al. Role of monocyte chemoattractant protein-1 in liver fibrosis with transient myeloproliferative disorder in down syndrome. Hepatol Commun. 2018; 2: 230–236. [PubMed: 29507898]
51. Xie J, et al. Macrophage migration inhibitor factor upregulates MCP-1 expression in an autocrine manner in hepatocytes during acute mouse liver injury. Sci Rep. 2016; 6 27665
52. Li S, et al. TSLP protects against liver I/R injury via activation of the PI3K/Akt pathway. JCI Insight. 2019; 4 e129013
53. Sawa Y, et al. Hepatic interleukin-7 expression regulates T cell responses. Immunity. 2009; 30: 447–457. [PubMed: 19285437]
54. Affò S, et al. CCL20 mediates lipopolysaccharide induced liver injury and is a potential driver of inflammation and fibrosis in alcoholic hepatitis. Gut. 2014; 63: 1782–1792. [PubMed: 24415562]
55. Abul-Husn NS, et al. A protein-truncating HSD17B13 variant and protection from chronic liver disease. N Engl J Med. 2018; 378: 1096–1106. [PubMed: 29562163]
56. Esmaili S, et al. Core liver homeostatic co-expression networks are preserved but respond to perturbations in an organism- and disease-specific manner. Cell Systems. 2021; 12: 432–445. e7 [PubMed: 33957084]
57. Bourgeois P, et al. Tricho-hepato-enteric syndrome mutation update: mutations spectrum of TTC37 and SKIV2L, clinical analysis and future prospects. Hum Mutat. 2018; 39: 774–789. [PubMed: 29527791]
58. Hartley JL, et al. Mutations in TTC37 cause trichohepatoenteric syndrome (phenotypic diarrhea of infancy). Gastroenterology. 2010; 138: 2388–2398. 2398.e1-2 [PubMed: 20176027]
59. Hiejima E, et al. Tricho-hepato-enteric syndrome with novel SKIV2L gene mutations: a case report. Medicine (Baltimore). 2017; 96 e8601 [PubMed: 29145277]
60. Fabre A, et al. SKIV2L mutations cause syndromic diarrhea, or trichohepatoenteric syndrome. Am J Hum Genet. 2012; 90: 689–692. [PubMed: 22444670]

61. Sinha NK, et al. EDF1 coordinates cellular responses to ribosome collisions. eLife. 2020; 9 e58828 [PubMed: 32744497]
62. Wu CC-C, Peterson A, Zinshteyn B, Regot S, Green R. Ribosome collisions trigger general stress responses to regulate cell fate. Cell. 2020; 182: 404–416. e14 [PubMed: 32610081]
63. Queck A, et al. Systemic MCP-1 levels derive mainly from injured liver and are associated with complications in cirrhosis. Front Immunol. 2020; 11: 354. [PubMed: 32218781]
64. Ambade A, et al. Pharmacological inhibition of CCR2/5 signaling prevents and reverses alcohol-induced liver damage, steatosis, and inflammation in mice. Hepatology. 2019; 69: 1105–1121. [PubMed: 30179264]
65. Baeck C, et al. Pharmacological inhibition of the chemokine CCL2 (MCP-1) diminishes liver macrophage infiltration and steatohepatitis in chronic hepatic injury. Gut. 2012; 61: 416–426. [PubMed: 21813474]
66. Teng K-Y, et al. Blocking the CCL2-CCR2 axis using CCL2 neutralizing antibody is an effective therapy for hepatocellular cancer in a mouse model. Mol Cancer Ther. 2017; 16: 312–322. [PubMed: 27980102]
67. Anstee QM, et al. Cenicriviroc for the treatment of liver fibrosis in adults with nonalcoholic steatohepatitis: AURORA Phase 3 study design. Contemp Clin Trials. 2020; 89 105922 [PubMed: 31881392]
68. Clark MM, et al. Diagnosis of genetic diseases in seriously ill children by rapid whole-genome sequencing and automated phenotyping and interpretation. Sci Transl Med. 2019; 11 eaat6177 [PubMed: 31019026]
69. Kumar P, Henikoff S, Ng PC. Predicting the effects of coding non-synonymous variants on protein function using the SIFT algorithm. Nat Protoc. 2009; 4: 1073–1081. [PubMed: 19561590]
70. Adzhubei IA, et al. A method and server for predicting damaging missense mutations. Nat Methods. 2010; 7: 248–249. [PubMed: 20354512]
71. Schwarz JM, Rödelsperger C, Schuelke M, Seelow D. MutationTaster evaluates disease-causing potential of sequence alterations. Nat Methods. 2010; 7: 575–576. [PubMed: 20676075]
72. Rentzsch P, Witten D, Cooper GM, Shendure J, Kircher M. CADD: predicting the deleteriousness of variants throughout the human genome. Nucleic Acids Res. 2019; 47: D886–D894. [PubMed: 30371827]
73. Quang D, Chen Y, Xie X. DANN: a deep learning approach for annotating the pathogenicity of genetic variants. Bioinformatics. 2015; 31: 761–763. [PubMed: 25338716]
74. Shamsani J, et al. A plugin for the ensembl variant effect predictor that uses MaxEntScan to predict variant spliceogenicity. Bioinformatics. 2019; 35: 2315–2317. [PubMed: 30475984]
75. Pertea M, Lin X, Salzberg SL. GeneSplicer: a new computational method for splice site prediction. Nucleic Acids Res. 2001; 29: 1185–1190. [PubMed: 11222768]
76. Richards S, et al. Standards and guidelines for the interpretation of sequence variants: a joint consensus recommendation of the American College of Medical Genetics and Genomics and the Association for Molecular Pathology. Genet Med. 2015; 17: 405–424. [PubMed: 25741868]
77. Vangipuram M, Ting D, Kim S, Diaz R, Schüle B. Skin punch biopsy explant culture for derivation of primary human fibroblasts. J Vis Exp. 2013; 77 e3779
78. Tang WJ. Blot-affinity purification of antibodies. Methods Cell Biol. 1993; 37: 95–104. [PubMed: 8255253]
79. Jao L-E, Wente SR, Chen W. Efficient multiplex biallelic zebrafish genome editing using a CRISPR nuclease system. Proc Natl Acad Sci USA. 2013; 110: 13904–13909. [PubMed: 23918387]
80. Bligh EG, Dyer WJ. A rapid method of total lipid extraction and purification. Can J Biochem Physiol. 1959; 37: 911–917. [PubMed: 13671378]

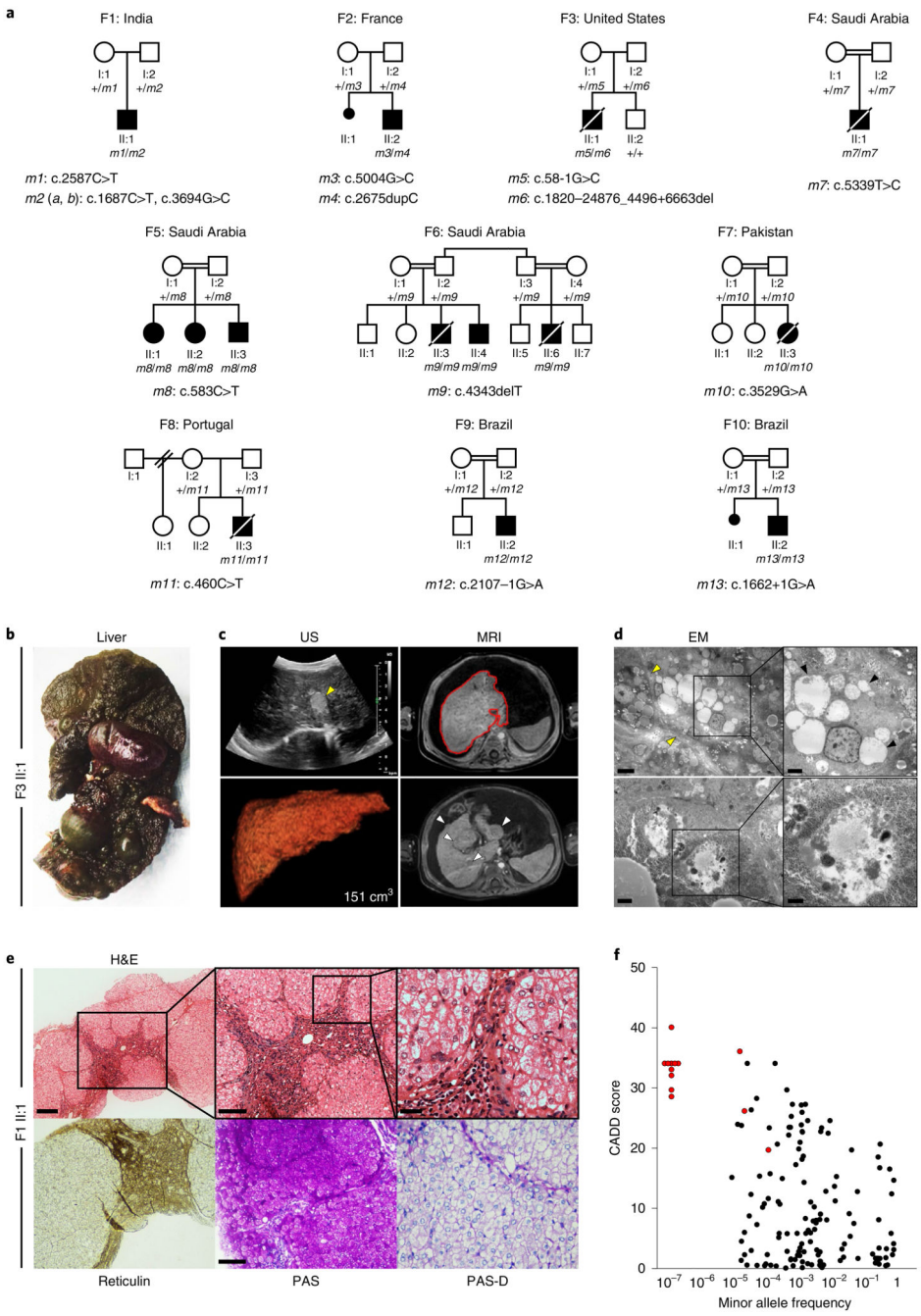

Fig. 1. Biallelic *FOCAD* mutations in 14 children diagnosed with pediatric liver disease.

a, Pedigrees of ten families segregating autosomal recessive liver disease. Filled black symbols indicate affected individuals. Crossed symbols indicate deceased individuals. Small black circles indicate miscarriage. Germline *FOCAD* variant coordinates are indicated below the pedigrees. Homozygous mutations are presented in bold. Compound heterozygous mutations are presented according to their parental origin. **b**, Explanted liver from patient F3-II:1 at 6 months showing collapsed lobules and severe cirrhosis. **c**, Abdominal ultrasound (US) and MRI from patient F3-II:1. US imaging (top left) showed a diffusely heterogeneous

Europe PMC Funders Author Manuscripts

liver and a focal hyperechoic mass of 1.5 cm in diameter (yellow arrow). MRI without contrast (top right) revealed the heterogeneity and multinodularity of the liver parenchyma (delineated by a red line). Larger nodules ranging from 0.5 to 1.5 cm (white arrows) were visible with Eovist contrast (bottom right). A three-dimensional (3D) reconstruction of the liver (bottom left) showed a small and irregular organ with a mildly nodular surface. **d**, Liver electron microscopy (EM) images from patient F3-II:1. Hepatocytes appeared large in size with visible pericellular fibrosis (top left, yellow arrows) and abundant vesicular steatosis (top right, black arrows). Enlarged lysosomes containing flocculent materials were also observed (bottom). Scale bars, 5 μm (top left), 1 μm (top right), 300 nm (bottom left) and 150 nm (bottom right). **e**, Liver biopsy from patient F1-II:1 at 17 months. H&E staining (top) revealed a marked cirrhotic pattern. Hepatocytes showed moderate swelling with pale cytoplasm (top right). Reticulin staining (bottom left) showed broad septal fibrosis. PAS staining (bottom middle) revealed high levels of intracytoplasmic glycogen in hepatocytes, which was readily digested by diastase (PAS-D, bottom right). Scale bars, 150 μm (top left), 100 μm (top middle), 50 μm (bottom middle) and 25 μm (top right). **f**, *FOCAD* is intolerant to genetic variation: minor allele frequency (*x* axis) and CADD score (*y* axis) of homozygous *FOCAD* coding variants found in gnomAD v.2.1.1 (black dots, $n = 135$) and those found in each of the ten families (red dots, $n = 13$).

Europe PMC Funders Author Manuscripts

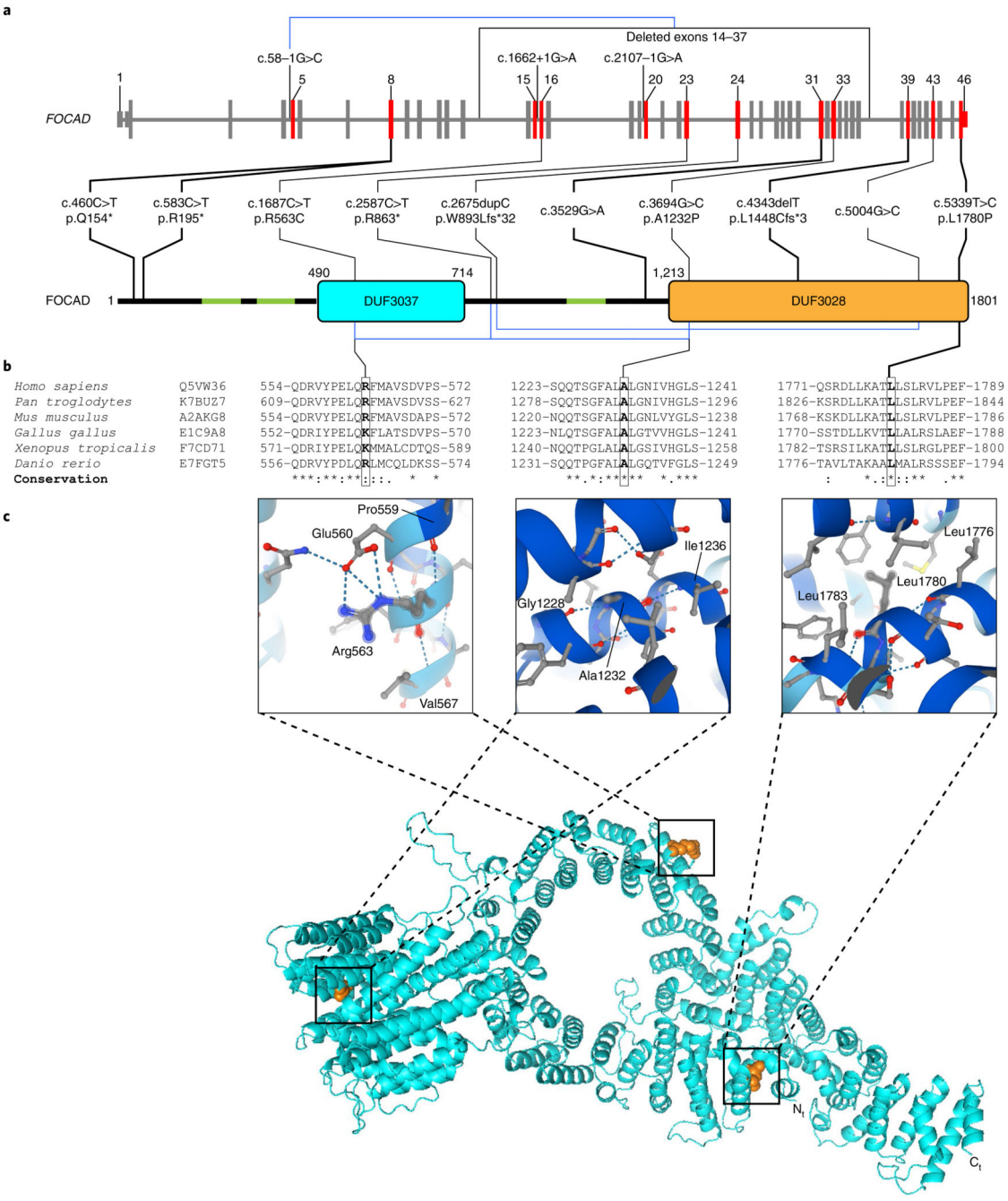

Fig. 2. FOCAD variants are predicted to be loss-of-function alleles.

a, Schematic diagrams of the genomic (top) and protein (bottom) structure of FOCAD in humans. The FOCAD protein contains two conserved domains of unknown function (blue, DUF3037; orange, DUF3028) and three predicted transmembrane domains (green). A total of 14 germline variants in *FOCAD* are indicated at the DNA and the protein levels. Homozygous mutations are shown in bold. Compound heterozygous mutations are linked by a blue line. **b**, Multiple sequence alignment for FOCAD protein in different species from fish to humans, showing the conservation of residues affected by missense mutations.

Europe PMC Funders Author Manuscripts

c, Predicted 3D conformation for human FOCAD as predicted by AlphaFold (v.2)[14]. The three residues affected by missense mutations Arg563, Ala1232 and Leu1780 are embedded in α-helices. Arg563 forms a hydrogen bond with Pro559 through its amino group, a hydrogen bond with Val567 through its carboxyl group and three hydrogen bonds with Glu560 through its side chain. Ala1232 forms a hydrogen bond with Gly1228 through its amino group and a hydrogen bond with Ile1236 through its carboxyl group, while the side chain remains free. Leu1780 forms a hydrogen bond with Leu1776 through its amino group and a hydrogen bond with Leu1783 through its carboxyl group, with its side chain free. N_t, N terminus; C_t, C terminus.

Europe PMC Funders Author Manuscripts

Europe PMC Funders Author Manuscripts

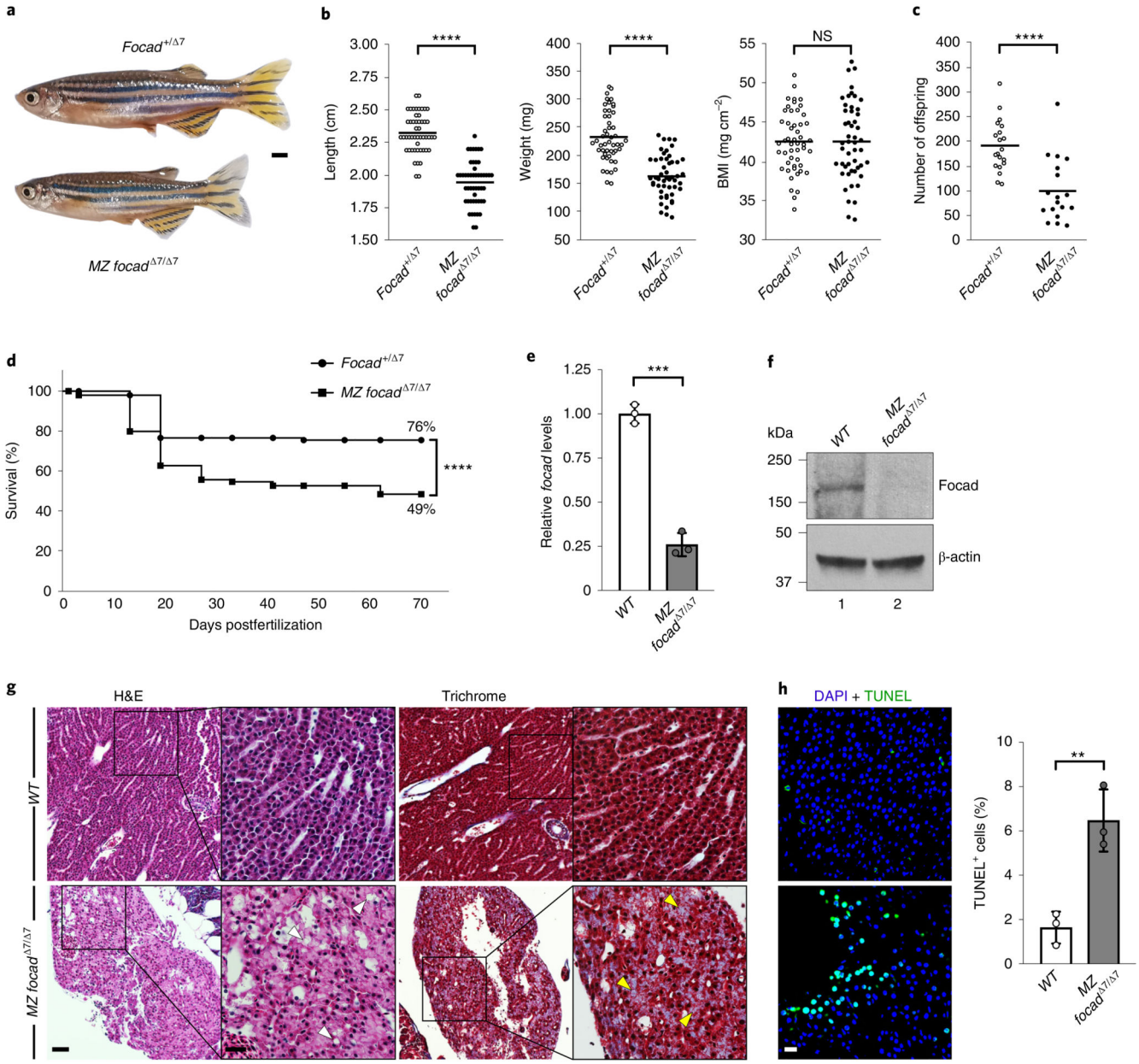

Fig. 3. *focad* loss in zebrafish compromises growth, fertility, lifespan and liver homeostasis, phenocopying the human syndrome.

a, Brightfield images of adult 3-month-old male zebrafish. *MZ focad*$^{\Delta 7/\Delta 7}$ fish are smaller in size compared with *focad*$^{+/\Delta 7}$ fish. Scale bar, 20 mm. **b**, Quantification of the body length, weight and BMI of *focad*$^{+/\Delta 7}$ ($n = 50$) and *MZ focad*$^{\Delta 7/\Delta 7}$ ($n = 50$) male zebrafish at 3 months of age. *MZ focad*$^{\Delta 7/\Delta 7}$ animals are proportionally smaller. ****$p < 0.0001$; NS, nonsignificant (two-tailed unpaired *t*-test). **c**, Quantification of the number of viable offspring from *focad*$^{+/\Delta 7}$ incrosses ($n = 20$) and *MZ focad*$^{\Delta 7/\Delta 7}$ incrosses ($n = 18$). *MZ focad*$^{\Delta 7/\Delta 7}$ mothers laid significantly fewer eggs. ****$P <$ 0.0001 (two-tailed unpaired *t*-test). **d**, Kaplan–Meier survival curves of *focad*$^{+/\Delta 7}$ ($n =$ 100) and *MZ focad*$^{\Delta 7/\Delta 7}$ ($n = 100$) zebrafish during 70 days. *MZ focad*$^{\Delta 7/\Delta 7}$ animals

showed a significant survival disadvantage. ****$P < 0.0001$ (Logrank Mantel-Cox test). **e**, Endogenous *focad* transcript levels were reduced by 75% in liver samples from *MZ focad*$^{\Delta 7/\Delta 7}$ 3-month-old male zebrafish. Fold change relative to *WT* is plotted as mean ± s.d. ($n = 3$ biologically independent liver samples). ***$P = 0.0001$ (two-tailed unpaired *t*-test). **f**, Western blot analysis of endogenous Focad protein in brain extracts from 3-month-old male zebrafish, using our custom-made antibody. Focad protein was not detected in the *MZ focad*$^{\Delta 7/\Delta 7}$ zebrafish. **g,h**, Histological analysis of paraffin-embedded liver sections from 3-month-old male zebrafish. **g**, *MZ focad*$^{\Delta 7/\Delta 7}$ livers presented with a heterogeneous and less compact parenchyma, with hepatocytes appearing more dissociated and of irregular shape. Hepatocellular cytoplasmic swelling with presence of vacuoles resembling hepatic lipidosis was noted by H&E staining (white arrows). Increased collagen content (blueish staining, yellow arrows) was revealed by Masson's trichrome staining. Scale bars, 50 μm (lower magnification) and 20 μm (higher magnification). **h**, Significantly increased TUNEL staining was detected in *MZ focad*$^{\Delta 7/\Delta 7}$ livers compared with *WT* livers. Left, Representative images. DAPI (blue), TUNEL (green). Scale bar, 20 μm. Right, Quantification of TUNEL^{+} cells. Data are plotted as mean ± s.d. ($n = 3$ biologically independent liver samples). **$P = 0.0061$ (two-tailed unpaired *t*-test). Unprocessed western blots are provided as source data.

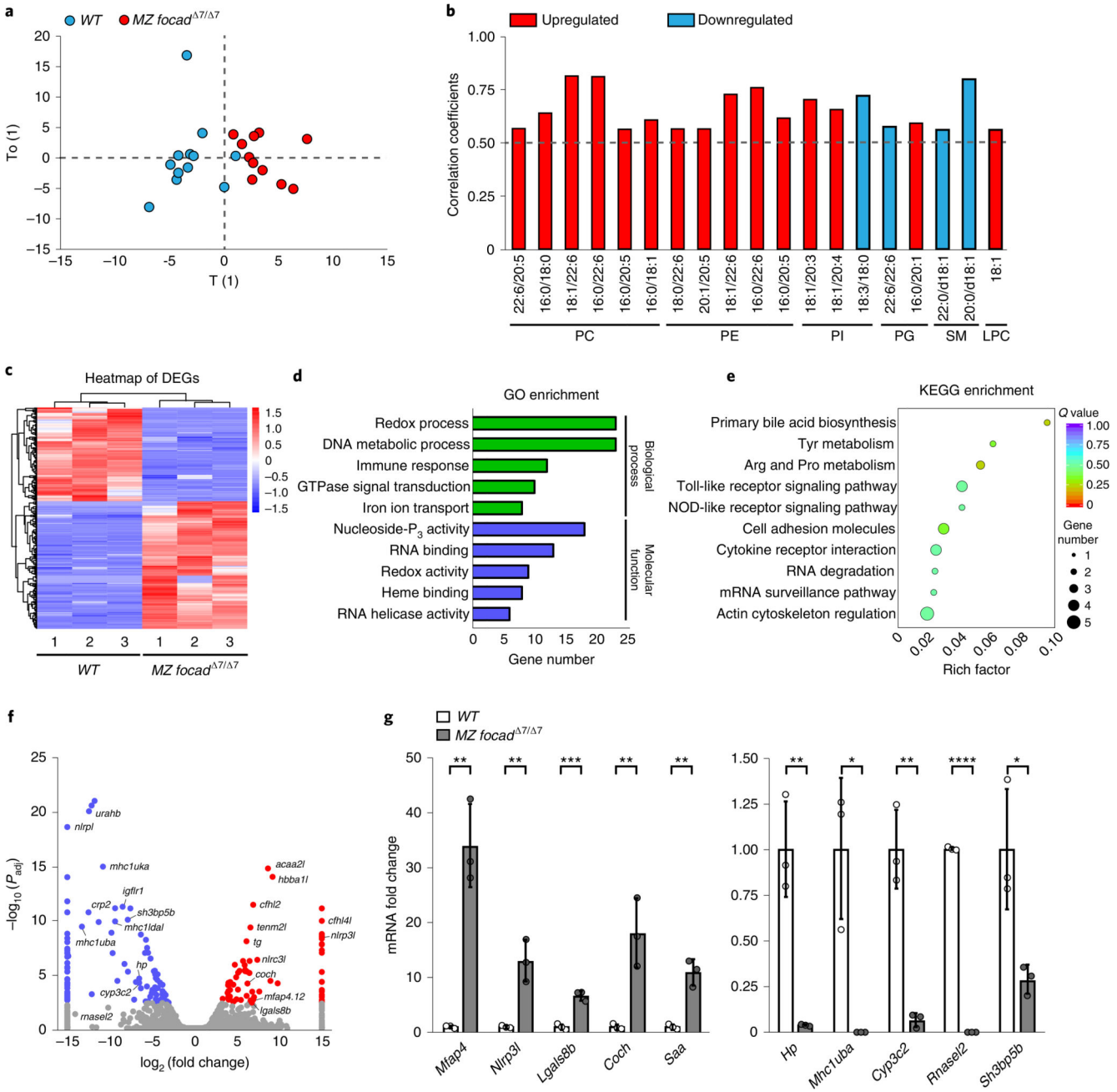

Fig. 4. *focad* knockout zebrafish livers show altered lipidomic and transcriptomic signatures.

a, OPLS-DA score plot from multivariate analysis of hepatic lipids in *WT* (n = 12) and *MZ focad*$^{\Delta 7/\Delta 7}$ (n = 11) male zebrafish of 3 months of age, showing separation between both genotypes. **b**, Correlation coefficient plot from the lipidomics analysis. Red bars, upregulation; blue bars, downregulation of lipid species in *MZ focad*$^{\Delta 7/\Delta 7}$ livers (n = 11) compared with *WT* livers (n = 12). PC, phosphatidylcholine; PE, phosphatidylethanolamine; SM, sphingomyelin; PI, phosphatidylinositol; PG, glycerophosphoglycerol; LPC, lysophosphatidylcholine. **c-f**, RNA-seq data from 3-month-old male zebrafish livers (n = 3). **c**, Heatmap showing the cluster analysis of DEGs in *MZ*

Europe PMC Funders Author Manuscripts

focad$^{\Delta 7/\Delta 7}$ versus *WT* livers. **d**, GO term enrichment analysis of the significant DEGs in *MZ focad*$^{\Delta 7/\Delta 7}$ livers. **e**, Bubble plot showing the KEGG pathway enrichment analysis of the significant DEGs in *MZ focad*$^{\Delta 7/\Delta 7}$ livers. The rich factor for each pathway (horizontal coordinates) was calculated as the ratio of the DEGs enriched in the pathway to the total number of genes annotated in the pathway. *Q* values were calculated with hypergeometric test. **f**, Volcano plot showing DEGs between *MZ focad*$^{\Delta 7/\Delta 7}$ and *WT* livers. Red dots, top 68 upregulated transcripts; blue dots, top 100 downregulated transcripts. The *P* values were calculated using two-tailed Wald test (DESeq) and corrected for multiple comparisons using Benjamini and Hochberg's approach. g, RT-qPCR quantification of the expression of some relevant DEGs (up, left; down, right) identified by RNA-seq using independent liver samples from 3-month-old male zebrafish. Results confirm the reliability of our RNA-seq data and provide further molecular evidence of the hepatic injury phenotype in *MZ focad*$^{\Delta 7/\Delta 7}$ fish. Fold change relative to *WT* is plotted as mean ± s.d. ($n = 3$ biologically independent liver samples). *$P < 0.05$ (*mhcluba*: 0.0108; *sh3bp5b*: 0.0214); **$P < 0.01$ (*mfap4*: 0.0017; *nlrp3l*: 0.0058; *coch*: 0.0094; *saa*: 0.0023; *hp*: 0.0031; *cyp3c2*: 0.0018); ***$P = 0.0008$; ****$P < 0.0001$ (two-tailed unpaired *t*-test).

Europe PMC Funders Author Manuscripts

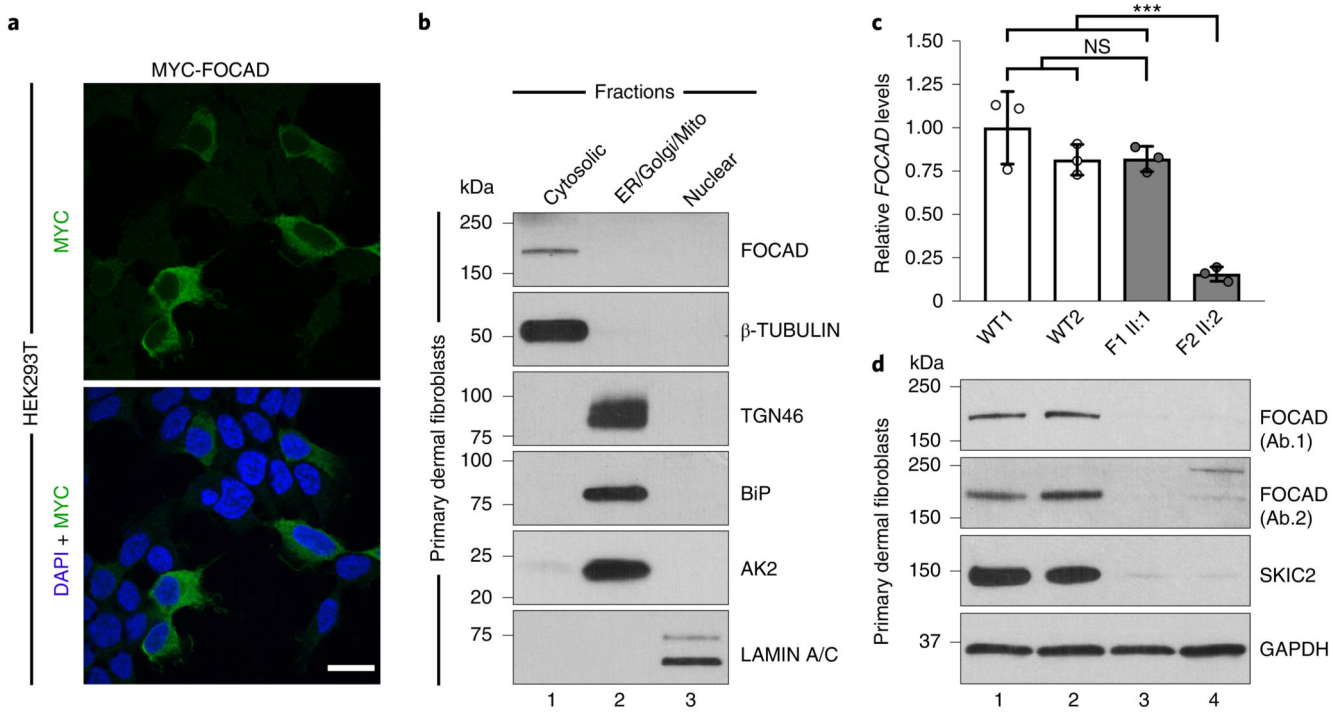

Fig. 5. FOCAD localizes in the cytosol and its absence in patient-derived primary dermal fibroblasts leads to reduced SKIC2 protein levels.

a, Immunofluorescence staining of anti-MYC (green) in HEK293T cells transfected with the pcDNA3.1-MYC-FOCAD construct. MYC-FOCAD showed a cytosolic localization. Scale bar, 20 μm. **b**, Western blot for FOCAD protein (Ab.1, custom-made antibody) using cytosolic, ER/Golgi/Mito and nuclear protein extracts from WT primary dermal fibroblasts. Endogenous FOCAD was detected exclusively in the cytosolic fraction. β-TUBULIN, cytosolic marker; TGN46, Golgi network marker; BiP, ER marker; AK2 (adenylate kinase), Mito marker; LAMIN A/C, nuclear marker. **c,d**, Endogenous FOCAD expression analysis at the mRNA and protein levels in primary dermal fibroblasts from F1-II:1 (p.Arg863*; p.Arg563Cys, p.Ala1232Pro) and F2-II:2 (p.Lys1668Asn; p.Trp893Leufs*32) patients and two unrelated controls (WT1, WT2). **c**, *FOCAD* RNA transcripts were significantly reduced in F2-II:2 but remained unaltered in F1-II:1 compared with controls. Fold change relative to WT1 is plotted as mean ± s.d. ($n = 3$ biological replicates). ***$P = 0.0007$; NS, nonsignificant (ordinary one-way-ANOVA with Tukey test for multiple comparisons). **d**, Western blot analysis of endogenous FOCAD (Ab.1, custom-made antibody; Ab.2, Invitrogen, catalog no. PA5-63051) and SKIC2 proteins. Results showed that FOCAD protein levels were almost negligible in both patient cell lines, while SKIC2 protein levels were also drastically reduced. Unprocessed western blots are provided as source data.

Europe PMC Funders Author Manuscripts

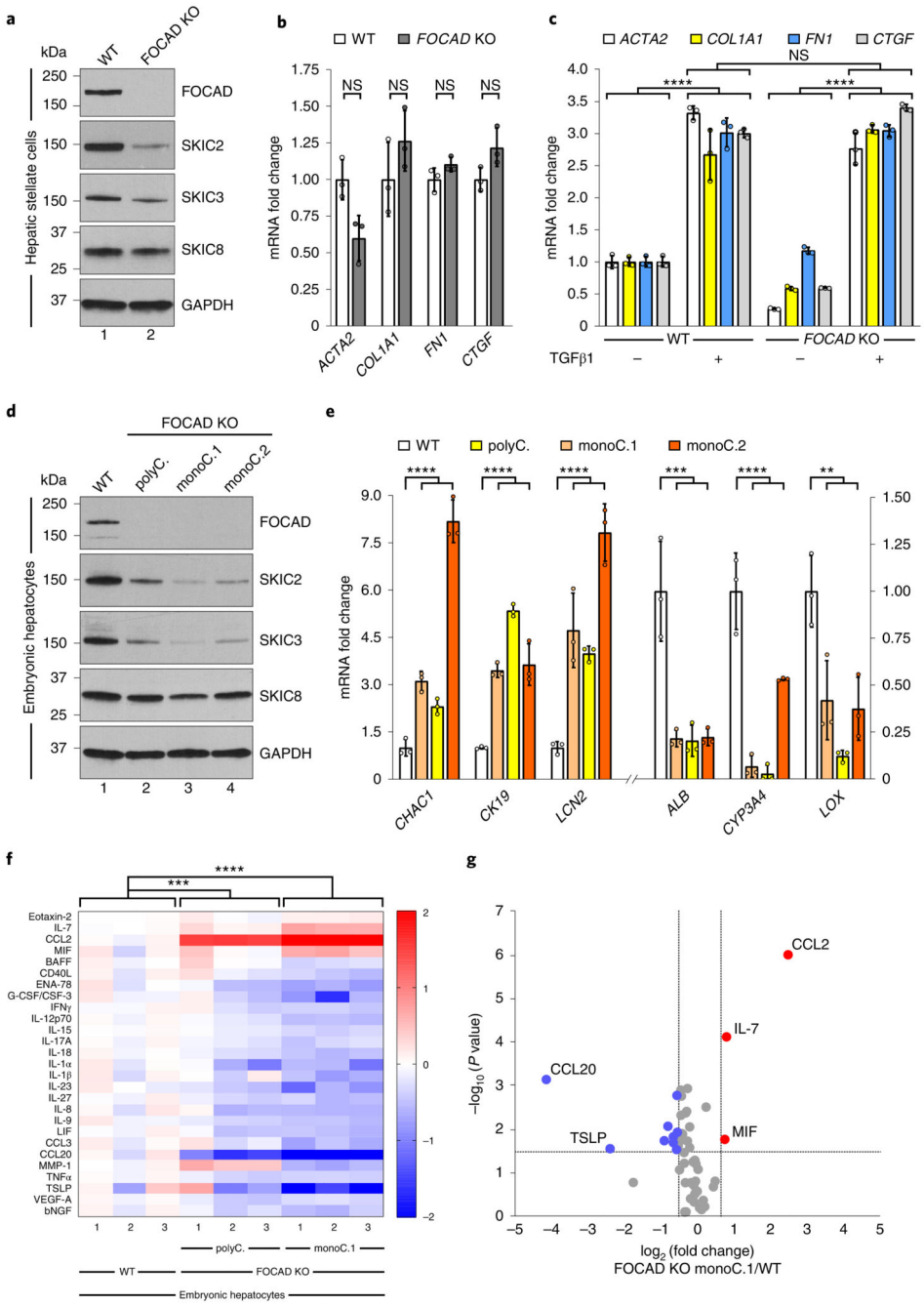

Fig. 6. Loss of FOCAD compromises the stability of the SKI complex, resulting in damaged hepatocytes.

a, Western blot analysis of endogenous FOCAD (Ab.2), SKIC2, SKIC3 and SKIC8 proteins in human hepatic stellate cells (LX-2 cell line). Decreased SKIC2 and SKIC3 protein levels were observed in the absence of FOCAD, whereas no overt difference was detected for SKIC8. **b**, Quantification of the expression of myofibroblast and ECM genes showed no alterations in the activation state of *FOCAD* knockout hepatic stellate cells. Fold change relative to WT is plotted as mean ± s.d. (n = 3 biological replicates). NS, nonsignificant

(two-tailed unpaired *t*-test). **c**, Both WT and *FOCAD* knockout hepatic stellate cells were responsive to TGFβ1 (2.5 $ngml^{-1}$ for 20 h), but there was no significant difference in the extent of the response between both genotypes. Data are presented as mean ± s.d. ($n = 3$ biological replicates). For the TGFβ1 treatment, fold change relative to the control condition for each genotype is plotted. For the control treatment data, fold change relative to WT is plotted. ****$P < 0.0001$; NS, nonsignificant (ordinary two-way ANOVA). **d**, Western blot analysis of endogenous FOCAD (Ab.2), SKIC2, SKIC3 and SKIC8 proteins in human embryonic hepatocytes (Hc3716-hTERT cell line). Absence of FOCAD resulted in reduced SKIC2 and SKIC3 protein levels, without affecting SKIC8. **e**, Loss of *FOCAD* expression in human embryonic hepatocytes led to the upregulation (left) and downregulation (right) of several genes involved in hepatocyte function, stress, regeneration and tumorigenesis. Fold change relative to WT is plotted as mean ± s.d. ($n = 3$ biological replicates). **$P = 0.0012$; ***$P = 0.0003$; ****$P < 0.0001$ (ordinary one-way ANOVA). **f**, Heatmap showing the Luminex cluster analysis of significantly dysregulated cytokines in the culture media of WT, FOCAD knockout polyclonal and FOCAD knockout monoclonal human hepatocyte cell lines. ***$P = 0.0004$; ****$P < 0.0001$ (ordinary two-way-ANOVA). **g**, Volcano plot showing differentially secreted cytokines between WT and FOCAD knockout monoclonal hepatocytes. The red dots represent the top three upregulated cytokines ($\log_2$(fold change) > 0.6, $-\log_{10}(P) > 1.5$); the blue dots represent the top eight downregulated cytokines ($\log_2$(fold change) < –0.6, $-\log_{10}(P_{adj}) > 1.5$). The *P* values were calculated using two-tailed unpaired *t*-test. polyC, polyclonal population; monoC.1, monoclonal population 1; monoC.2, monoclonal population 2. Unprocessed western blots are provided as source data.

Europe PMC Funders Author Manuscripts

Table 1

Clinical comparison between *FOCAD* deficiency syndrome and THES type 1 and type 2

	***FOCAD* deficiency syndrome**	**THES type 1 (MIM614602)**	**THES type 2 (MIM222470)**
Gene	*FOCAD* (MIM614606)	*SKIC2* (MIM600478)	*SKIC3* (MIM614589)
Recessive inheritance	+	+	+
Mutation type	Loss-of-function	Loss-of-function	Loss-of-function
Total number of patients	14	31 (ref. [57])	65 (ref. [57])
Clinical synopsis			
Hepatic abnormalities	100%	88%	51%
Hepatomegaly	71.4%	+	+
Cirrhosis	71.4%	+	+
Elevated hepatic enzymes	71.4%	+	+
Cholestasis	35.7%	+	+
Elevated hepatic iron concentration	21.4%	+	+
IUGR	64.3%	86%	70%
Diarrhea	57.1%	100%	100%
Platelet/coagulation abnormalities	50.0%	33%	14%
Cardiac abnormalities	42.9%	36%	33%
Supravalvular aortic stenosis	7.1%	+	+
Ventricular septal defect	7.1%	+	+
Craniofacial abnormalities	35.7%	84%	84%
Skin abnormalities	21.4%	53%	39%
Hair abnormalities	7.1%	89%	95%
Immune deficiency	7.1%	44%	56%

Data related to both types of THES were extracted from Bourgeois et al.[57]; +, presence of phenotype with unknown prevalence.